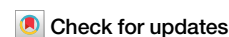


<https://doi.org/10.1038/s41529-024-00467-5>

Complementary corrosion protection of cast AlSi7Mg0.3 alloy using Zr-Cr conversion and polyacrylic/siloxane-silica multilayer coatings

Peter Rodič[✉], Barbara Kapun & Ingrid Milošev[✉]

Aluminium cast alloy AlSi7Mg0.3 is a lightweight metal commonly used in automotive, aeronautical and mechanical applications. It has good corrosion resistance but, under harsh operative conditions, would benefit from additional protection. In this study, a corrosion-protective multilayer coating system for AlSi7Mg0.3 based on hexafluoro-zirconated trivalent chromium coating (Zr-CrCC) and polyacrylic/siloxane-silica (PEHA-SS) coating was developed. The Zr-CrCC was formed by immersion of the substrate in a commercial conversion bath (SurTec® 650). PEHA-SS synthesis was based on organic precursors (2-ethylhexyl acrylate and [3-(methacryloyloxy)propyl]trimethoxysilane) and an inorganic precursor, tetraethyl orthosilicate. After deposition on AlSi7Mg0.3, each coating was first characterised individually, followed by the analysis of the multilayer using scanning electron microscopy and energy-dispersive X-ray spectroscopy. The adhesion of the coatings was evaluated with a cross-hatch cut test. The corrosion studies in sodium chloride solution using electrochemical impedance spectroscopy and salt spray testing showed that the multilayer system is superior to individual Zr-CrCC and PEHA-SS coatings. After 4 months in 0.1 M NaCl, the multilayer-coated samples exhibited the impedance at 10 mHz in the range of $G\Omega\text{ cm}^2$, while scribed samples withstood the corrosion attack in a salt spray chamber for one week. Thus, albeit only about 100 nm thick, the Zr-CrCC deposited between the substrate and a 9-micrometre thick barrier sol-gel PEHA-SS coating acts as an active corrosion protection interlayer and contributes to the overall protectiveness of the multilayer system.

The relevant casting characteristics of alloys 3xx.x series are the main reasons that almost 90% of all cast aluminium alloys produced belong to this series¹. These alloys contain silicon, copper and/or magnesium as alloying elements¹. Alloys containing silicon have improved castability, wear resistance, and reduced melting point. Silicon and magnesium form the Mg₂Si intermetallics (IMs), contributing to better strength², but alloys with a greater proportion of copper and magnesium have lower corrosion resistance^{2–4}. The most common cast alloy AlSi7Mg0.3 (also classified as EN AC-42100)² is used in industry for various parts of engines, automobile wheels, aircraft parts, housings, compressors and pumps.

Over the last few decades, many research studies in corrosion protection have focused on developing effective coatings to replace environmentally hazardous chromate conversion coatings containing

chromium(VI)^{5–8}. In the last twenty years, various environmentally acceptable and efficient corrosion protective conversion coating systems based on manganese^{9,10}, titanium^{11,12}, cerium^{13–16}, trivalent chromium process (TCP)^{17–20}, and zirconium^{12,21–30} have been investigated. The zirconium-based coatings (ZrCCs) are already commercialised¹². When analysing the literature data and commercial products, it should be distinguished that some ZrCCs contain only Zr-bearing components, while others also contain trivalent chromium salt. ZrCC conversion baths most often contain hexafluoro zirconic acid (H_2ZrF_6)^{12,21,22,25,27–29}, but in some studies, potassium fluorozirconate (K_2ZrF_6)²⁶, and H_2ZrF_6 and hexafluorotitanic acid (H_2TiF_6) were used^{29,31}. Some products also contain a small amount of cupric ions^{27,28} for stimulating the precipitation of the coating, phosphate²⁶ or borate ions²¹. TCP baths contain, usually in addition to the Zr-bearing component, a

trivalent chromium salt (≤ 5 wt.%) to form a Zr-Cr-rich oxide coating on the metal substrate^{17–20}. The terminology in the literature is not very strict, so the term ZrCC has often been used when the coating contained Zr and Cr-bearing components, and the term TCP has often been used albeit the coating contained not only Cr(III) but also Zr-bearing component. The terms ZrCCs and TCP are thus used generically, often not specifying the actual coating composition, which can sometimes be misleading.

The formation of the conversion coating can be generally divided into the following steps: (i) degreasing using an alkaline cleaner to remove organic contaminants and part of a naturally grown oxide layer on the aluminium surface, (ii) desmutting of the smut layer formed during alkaline cleaning to remove some of the insoluble intermetallic particles, and at the same time, to passivate aluminium surface in the presence of HNO_3 , and (iii) coating formation in the conversion bath^{24–26,32,33}. The deposition of conversion coating is a pH-dependent process. Metal substrate dipped into a conversion bath containing Zr-bearing species becomes covered by Zr-hydrated oxide precipitated on the metal surface once the pH reaches the value required for precipitation (usually around $\text{pH} \approx 4$). This process is the most pronounced at the cathodic sites where, due to oxygen reduction reaction and concomitant OH^- formation, the pH rises to the values suitable for the precipitation of Zr(IV) hydroxide ($\text{ZrO}_2 \times 2\text{H}_2\text{O}$), which is then stable up to highly alkaline pH values^{12,21,25,30,34,35}. In the case of conversion baths containing both zirconium and trivalent chromium, the precipitation of Cr(III) hydroxide proceeds at similar pH values³⁵.

The ZrCCs deposited on the aluminium alloys enhance the corrosion properties^{24,25} and adhesion of the upper organic layer^{10,36–38}. Namely, the role of the conversion coating is not solely corrosion protection but also adhesion to the upper organic layer, as in industrial applications, the coating system consists of the primer, organic and/or top layers. For that reason, several studies have focused on the effect of adhesion of ZrCCs as an interlayer between metal and organic coatings. The variety of combinations investigated is very broad. As substrates, mainly steels, galvanised steels and wrought Al alloys were used. The general conclusion is that the ZrCC interlayer coating, albeit being only 50–150 nm thick, improves the adhesion strength of the several tens of micrometres thick upper organic coating to the underlying metal substrate; this finding was ascribed to conversion coating providing stronger bonding, increasing the surface roughness and reducing the cathodic disbondment of the organic coating by inhibiting the formation of large water aggregates. The adhesion is improved under both dry and wet conditions. These issues were reported for mild steel^{36,39,40}, cold-rolled steel⁴¹, carbon steel⁴² and galvanised steel³¹ using ZrCC coatings prepared from H_2ZrF_6 and H_2TiF_6 ³¹, Jiuhe Zr solution⁴¹ and MAVOM 1742 coating⁴². As organic layers, epoxy coatings^{39–42}, epoxy-containing ZnAl polyphosphate pigments³⁶ and polyester-based resins³¹ were used. As additives to ZrCC, Zn sulphate⁴⁰ or various organic components were used³¹. The former acted as anti-corrosion pigments, whereas the latter initially improved the interfacial stability of conversion coating-treated substrates; however, in the long term, organic additives were shown to be detrimental to polyester coil coat adhesion.

The combination of conversion and organic coatings was investigated on various wrought Al alloys: AA1050⁴³, AA1060⁴⁴, AA6016⁴⁵, AA6060^{46,47}, AA6063^{48,49} and AA7A52³⁸. As Zr-based interlayers, conversion coatings prepared from H_2ZrF_6 ⁴³, H_2ZrF_6 and H_2TiF_6 ⁴⁵, H_2ZrF_6 , H_2TiF_6 , sodium vanadate and phosphoric acid^{44,48}, potassium hexafluoro zirconate, hexafluorotitanate and amino trimethylene phosphonic acid (ATMP)³⁸ and commercial Zr/Ti Alodine 5200® (Henkel)⁴⁹ were used. In addition, cerium-based conversion layers combined with organic layers were also studied^{46,47}. As organic layers, polyester coating⁴⁷, water-based polyurethane resin⁴⁴, epoxy^{26,48}, polyvinylidene fluoride (PVDF) and acrylic resin⁴⁹, acrylic resin⁴⁵ and epoxy/polyamide⁴³ were used. In one study, a thin ZrO_2 sol-gel layer was applied above the Ce-based conversion coating⁴⁶.

The presence of ZrCC as an interlayer between the substrate and organic coatings also improves the corrosion properties. If we focus more on the Al-based substrates, it was reported that when prepared with the Ti/Zr/V conversion interlayer, polyurethane coating exhibited excellent corrosion

resistance and eliminated the post-film washing step, thus simplifying the process⁴⁴. Ti/Zr interlayer between the AA7A52 substrate and epoxy coating demonstrated very good results in the salt spray chamber, ascribed to the conversion layer's barrier properties³⁸. Another study reported that the conversion coating (Alodine 5200®) achieved poor results in the salt spray chamber because of its small thickness of only 20 nm, which is insufficient to produce a barrier effect⁴⁹. However, when combined with a PVDF/acrylic resin, the corrosion resistance of the system as a whole improved⁴⁹. Similar results were published also for ZrCC/epoxy-polyamide-coated AA1050⁴³.

It was reported in previous publications that ZrCCs prepared from H_2ZrF_6 on wrought aluminium alloy AA3005 have the ability of so-called self-sealing, i.e. improvement of protective properties of the coatings with prolonged immersion in sodium chloride solution^{24,25}. The self-sealing was explained by the transformation of $\text{ZrF}_4/\text{ZrO}_x\text{F}_y$ to $\text{ZrO}_2 \cdot 1.2\text{H}_2\text{O}_{(s)}$, i.e. progressive loss of fluoride from the coating and densification of the Zr-oxide layer^{24,25}. Similar properties were noted for the commercial hexafluoro-zirconate trivalent chromium coating SurTec 650® in sodium chloride solution and simulated acid rain²⁴. Compared to wrought aluminium alloys, relatively little is known about the electrochemical performance of conversion coatings on cast alloys^{14,50}.

Given these considerations and the overview of the literature studies given in the above text, it can be stated that corrosion and adhesion research study based on ZrCCs on cast aluminium alloys would bring novel results, not only for the individual coating but also in combination with organic overlayer, i.e. in a multilayer system. As Zr-based conversion coating, the commercial hexafluoro-zirconate trivalent chromium coating SurTec 650® was used (denoted as Zr-CrCC). Instead of commonly used organic coatings, usually several tens of micrometres thick, we explored a much thinner hybrid sol-gel coating. In our previous study, a polyacrylic/siloxane-silica coating (abbreviated PEHA-SS) was developed using tetraethyl orthosilicate (TEOS) as an inorganic precursor, and organically modified silane precursor [3-(methacryloyloxy)propyl]trimethoxysilane (MAPTMS) and an organic monomer 2-ethylhexyl acrylate (2-EHA)⁵¹. The nine micrometres thick PEHA-SS coating achieved durable corrosion (barrier) protection for the cast AlSi7Mg0.3 alloy in 0.1 M NaCl during the first four months of immersion or under accelerated corrosion conditions in a Machu chamber containing NaCl, acetic acid, and hydrogen peroxide at 37 °C⁵¹. The coating synthesis and characterisation details are given in our previous publication⁵¹.

This study aimed to research the individual coatings (Zr-CrCC and PEHA-SS) and a combination of both on cast aluminium alloy AlSi7Mg0.3 (Supplementary Figure 1). This particular combination has not been investigated in the literature, mainly focusing on combining various ZrCCs and organic coatings on steels or wrought Al alloys. The study's rationale and experimental approach is thus to combine two methodologies on cast AlSi7Mg0.3 alloy and obtain a protective system with improved interfacial properties gained through SurTec 650® Zr-CrCC and efficient barrier properties gained through environmentally suitable sol-gel PEHA-SS coating. The coatings' characterisation was assessed using scanning electron microscopy (SEM) coupled with energy-dispersive X-ray spectroscopy (EDS), adhesion evaluation and corrosion testing in 0.1 M NaCl and salt spray chamber.

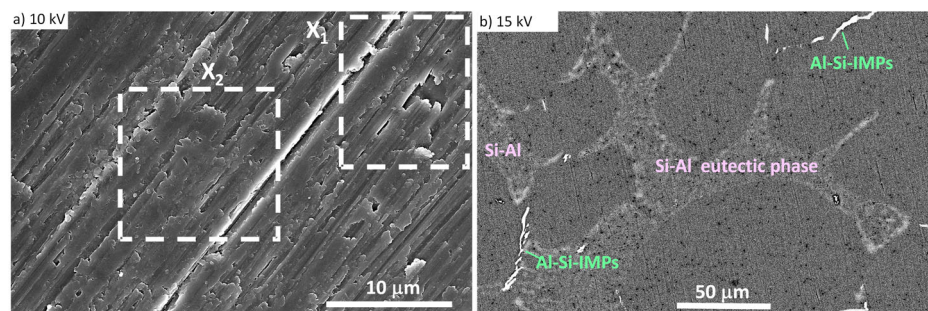
Results and discussion

Preparation of Zr-Cr conversion coating

The deposition of the Zr-Cr conversion coating consists of three steps: i) degreasing by immersion of the samples in an alkaline cleaning solution, ii) desmutting in an acidic solution and iii) surface passivation using the zirconium conversion process. After each step, the samples were rinsed with deionised water and dried. A detailed procedure of individual steps of Zr-CrCC deposition is given in the Methods section.

Figure 1a shows the SEM image of the ground alloy surface recorded using a secondary electrons (SE) detector. Cast AlSi7Mg0.3 alloy has high hardness (Brinell hardness ~ 55 HBW)³; therefore, the mechanical grinding with SiC paper left longitudinal marks on the surface. The EDS analysis is given in Table 1, revealing that x_1 belongs to the α -Al matrix consisting

Fig. 1 | SEM images of ground AlSi7Mg0.3. SEM images of ground non-coated AlSi7Mg0.3 surface recorded using (a) 10 kV and secondary electrons (SE) detector and (b) 15 kV and circular backscatter detector (CBS). In the SE image, x_1 denotes the matrix, and x_2 is the intermetallic particle. EDS results of the marked areas are given in Table 1. The heterogeneous structure is better visible in the CBS image, where different phases are noted. More details are given in ref. 4.



mainly of Al with a small amount of Si (1.9 at.%). Site x_2 refers to the intermetallic particle (IMP) containing Mg (0.9 at.%) and approximately ten times more Si than at the matrix (14.5 at.%) (Table 1). In contrast to the SE SEM image on the ground surface given in Fig. 1a, the image in Fig. 1b was recorded on the polished surface using a circular scattered electrons (CBS) detector. The heterogeneity of the surface is more pronounced than in Fig. 1a. A typical microstructure of AlSi7Mg0.3 alloy consists of an α -Al matrix, eutectic phase and intermetallic particles. The patterned area is a eutectic phase containing more than 60 at.% of Si and the rest of Al and Cr⁴. Bright intermetallic particles refer to Al-Si-based IMPs. In AlSi7Mg0.3 alloy, there are several types of IMPs: Al-Si-Mg, Al-Si-Mg(Fe), Al-Si-Fe-Mn and Al-Si-Fe-Mn(Mg)^{4,25}. The presence of Mg-rich intermetallics can reduce the corrosion resistance of the alloy compared to aluminium matrix^{3,16,25,52,53}.

Figure 2a–c present the SEM images of the ground AlSi7Mg0.3 sample coated with Zr-CrCC; images were recorded in CBS mode using different magnifications. The coverage of the Zr-CrCC was not homogeneous (Fig. 2a). Three regions are recognised, differing in the composition and thickness of the coating (detailed in Fig. 2b). The first characteristic regions are several micrometres broad areas of irregular shape (exampled by x_3 and x_6). When analysed using 10 kV acceleration voltage and higher magnification (Fig. 2a), it seems that no coating was formed since only the longitudinal grinding marks of the underlying substrate were visible.

EDS analysis (Table 1) of areas x_3 and x_6 (coated sample, Fig. 2) and x_1 (non-coated sample, Fig. 1a) confirmed the similar compositions comprised mainly of Al and a small amount of Si and O. Higher magnification (Fig. 2b) revealed the presence of a thin layer in these areas (exampled by x_6), which could not be observed when imaged at smaller magnification (Fig. 2a). However, EDS analysis at 10 kV (area x_6) still did not detect any element originating from the coating.

In contrast, when using the smaller voltage of 5 kV, Zr and F were detected also in these areas (area x_6 , Fig. 2c, Table 1). This discrepancy in the identification of coating elements is due to different analysis depths at 5 kV and 10 kV. Namely, the analysis depths are 300 and 1000 nm, respectively.

Table 1 | The composition (at.%) of the marked areas noted in Fig. 1a and Fig. 2 obtained by the EDS analysis

Spot	Composition (at. %)						
	Al	O	Si	Mg	Zr	Cr	F
x_1	91.1	7.0	1.9	-	-	-	-
x_2	76.4	8.2	14.5	0.9	-	-	-
x_3	96.4	2.3	1.3	-	-	-	-
x_4	78.9	11.2	5.0	-	2.3	1.2	1.4
x_5	47.3	17.3	27.0	0.3	4.0	1.9	2.2
x_6	96.4	2.2	1.4	-	-	-	-
x_7	82.8	11.2	1.5	-	2.1	1.1	1.3
x_8	47.5	19.2	23.0	-	5.1	2.7	2.5
x_9	87.4	7.4	1.6	-	2.2	-	1.4

The analysis depth was assessed using a Monte Carlo-based simulation; details are given in Supplementary Figure 2. The second observation is that only Zr and F, not Cr, were detected at 5 kV. Cr cannot be unambiguously identified under these conditions because, in contrast to Zr, its most intense peak is above 5 kV. $K\alpha$ and $L\alpha$ peaks for Zr are at 15.7 keV and 2.0 keV, respectively. $K\alpha$ and $L\alpha$ peaks for Cr are at 5.4 keV and 0.57 keV, respectively, which means that chromium's most intense peak cannot be identified when using an acceleration voltage of 5 kV (Cr $L\alpha$ peak at 0.57 keV is partially overlapping with the $K\alpha$ peak of O at 0.525 keV). Therefore, Cr can be detected reliably only when the EDS analysis is performed at 10 kV, while Zr can be detected at 5 kV. Notably, the concentration of Al originating from the underlying substrate is high (Table 1) due to a nanometric-size Zr-CrCC thickness and a micrometre-deep EDS analysis depth.

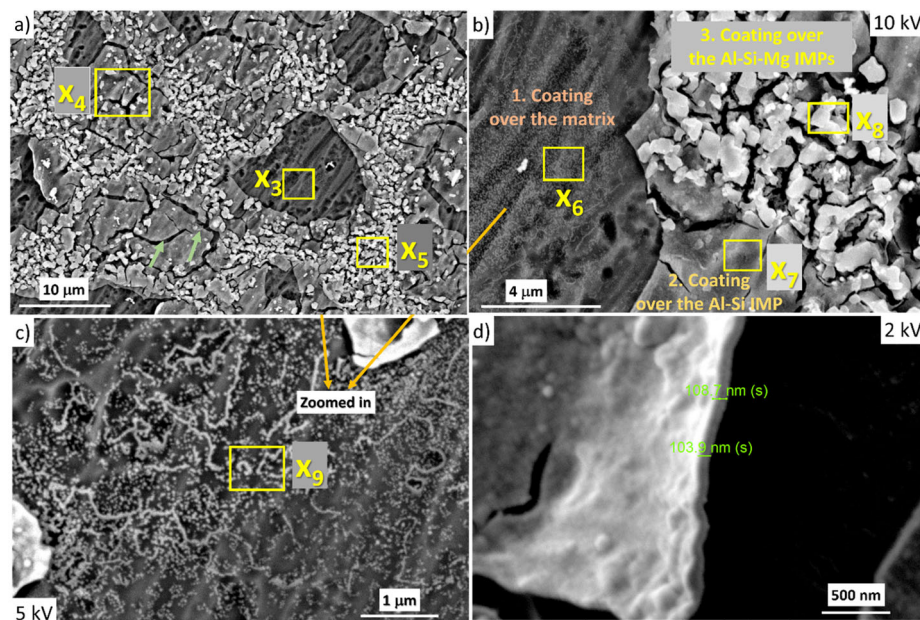
The second characteristic region refers to the rest of the surface visibly covered by the coating (areas x_4 and x_7 , Fig. 2a, b). EDS analysis of these sites detected Zr, Cr, F, and higher O concentrations (Table 1). The concentration of Zr doubled that of Cr, and the concentrations of Cr and F in the coating were similar. The concentration of O was more prominent than on the non-coated sample, and the concentration of Al was reduced to about 80 at.%. The coating formation suppressed the detection of Al from the substrate. Another important issue concerned the concentration of Si, which is at an area of x_4 considerable (5 at.%). The origin of Si is from the IMPs of the underlying substrate (Fig. 1); this result indicates that the coating formed above the Al-Si containing IMPs (areas x_4 and x_7) was much thicker than when formed above the α -matrix (areas x_3 and x_6).

The third characteristic area refers to agglomerated grain-like products formed on the coating (exampled by areas x_5 and x_8 , Fig. 2a, b). The grains are several hundred nanometres up to micrometre-sized. The coating thickness further increased in this area since the grains were much brighter in the CBS image than the underlying coating (i.e. areas x_4 and x_7). Indeed, EDS analysis detected higher amounts of Zr, Cr and F (Table 1). In addition, Mg was detected, along with a high Si concentration of 23 and 27 at.%, i.e. more than five times larger than in the homogeneous coating (areas x_4 and x_7). Considering the high Si contents detected, the parts of the coating growing above the area rich in Si (and Mg) are thicker and more abundant than those growing above areas with less Si or α -Al matrix. Notably, the concentration of Al was decreasing in the order $x_3, x_6 > x_4, x_7 > x_5, x_8$. The thickness of the Zr-CrCC coating increased in the reverse order. The coating thickness determined at the interface between the first and the second layer is around 100 nm (Fig. 2d). Above the matrix (x_3), the coating is probably a few tens of nanometres thick, reaching above 100 nm in agglomerated parts (x_5). Due to the small thickness of Zr-CrCC on the alloy surface, the adhesion cannot be evaluated with a cross-cut test according to the ASTM D3359–23 standard (see below).

During coating formation and growth, some micro-cracks appeared (arrows in Fig. 2a). This observation is quite common for conversion coatings; the shrinkage in volume induced by tensile stresses was particularly pronounced at thicker coatings, leading to cracking^{25,37}. Another reason for micro-cracking may be dehydration during drying in the SEM chamber.

The inhomogeneity of the coating coverage indicates that its formation proceeded laterally across the surface, being thicker at some sites at the alloy

Fig. 2 | Circular backscatter electron (CBS) SEM images of AlSi7Mg0.3 surface coated with Zr-CrCC. a, b Three characteristic regions of coating formation are recognized: above matrix (x_3 and x_6), above Al-Si IMPs (x_4 and x_7) and Al-Si-Mg IMPs (x_5 and x_8). **b** details area in **(a)** where all three regions are presented. Squares x_3 – x_9 indicate the areas where EDS analyses were performed with composition in atomic percentages (at.%). The results of EDS analysis are given in Table 1. Green arrows in **(a)** show cracks in the coating. **d** The coating thickness was determined between regions x_3 and x_5 at the interface area. SEM/EDS analyses were conducted at **a, b** 10 kV, **c** 5 kV and **d** 2 kV.

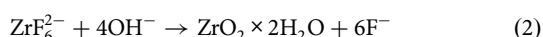


surface. As described above, the inhomogeneity of the coating thickness and composition are related to the inhomogeneity of the underlying substrate (Figs. 1, 2); it is the thinnest above the α -matrix (x_3), increases above the Al-Si-IMP (x_4) and is the largest above Al-Si-Mg-containing IMPs (x_5). These regions differ in their electrochemical activity as well. In heterogeneous alloys like Al alloys, IMPs represent sites of increased anodic or cathodic activity; notably, due to the ongoing selective dissolution of individual elements from the IMP, the activity can change from anodic to cathodic during immersion in chloride solution⁵⁴. In Al-Si-Mg alloys, IMPs containing Al, Si and Mg are subject to selective dissolution of the less noble metal (Mg or Al). This process depends on the pH; Al and Mg are selectively dissolved in acidic (Al, Mg) and near-neutral solutions (Mg), leaving behind Si-rich remnants, which then serve as a cathode^{54,55}. The surrounding α -Al matrix acts as an anodic site.

Cathodic reaction at the local cathodic sites, in this case Si-containing IMPs, is represented by reaction (1):



Considering the formation of areas of different thicknesses and morphologies (Fig. 2), it is reasonable to assume that IMPs containing more silicon act as a stronger cathode, readily leading to increased pH (reaction 1) and faster precipitation of Zr- and Cr-(hydr)oxides. Namely, locally increased pH on the micro-cathodic sites results in the hydrolysis of the soluble fluorometalate precursor species in the conversion bath³⁴. According to thermodynamic data, the pH values at which the conditions for the precipitation of hydrated metal oxide coating (e.g., $\text{ZrO}_2 \times 2\text{H}_2\text{O}$) are established are still in the acidic range, i.e., between 2 and 4–4.5, depending on the concentration of Zr-bearing species³⁴. Using the SurTec® ST650 conversion bath with pH = 3.9, the pH conditions at which the deposition of the coating at the metal surface are readily achieved. In general, the deposition of Zr(IV) hydroxide from the hexafluorozirconic acid bath proceeds according to reaction (2)³⁴.



Once deposited, Zr(IV) hydrated oxide is the most Zr-stable species at higher pHs³⁴. In addition to the Zr-bearing component, the SurTec® ST650 also contains trivalent Cr salt, resulting in incorporating both Zr and Cr in the conversion coating, as shown by EDS analysis (Table 1). The deposition

of Cr(III) hydroxide is feasible at the pH of the conversion bath. The formation of trivalent Cr hydr(oxide) along Zr(IV) hydr(oxide) was identified previously by X-ray photoelectron spectroscopy (XPS)^{17–20,24,56,57}. At pH around 4, the deposition of Ce^{3+} ions proceeds according to the reaction (3):



As shown by EDS analysis, the Zr-CrCC also contains fluoride (Table 1), as observed in previous studies^{24,25}. The coating can be, therefore, described by a Zr-Cr-(hydro)oxide or Zr-Cr-(hydro)oxyfluoride.

The corrosion behaviour of bare and Zr-CrCC-coated alloy was investigated by measuring electrochemical impedance after one hour of immersion. The selected representative Bode plots shown in Fig. 3 confirmed the differences in the corrosion resistance between ground non-coated and Zr-CrCC-coated samples in a corrosive medium of 0.1 M NaCl.

The Bode plot of impedance magnitude (Fig. 3a) showed the typical behaviour of a ground non-coated AlSi7Mg0.3 sample. For comparative purposes, the general measure of corrosion resistance can be represented by the value of $|Z_{10\text{ mHz}}|$ in the low-frequency (0.01 Hz) region (Fig. 3a). After 1 h of immersion, the $|Z_{10\text{ mHz}}|$ was $\sim 22\text{ k}\Omega\text{ cm}^2$, reflecting relatively low corrosion resistance. The phase angle plot showed the maximum phase angle of -79° at 23 Hz (Fig. 3b). This phenomenon is attributed to the forming of an aluminium oxide/hydroxide layer on the surface with some pores and defects allowing diffusion paths for corrosive species. These also can be reflected as a minimum phase angle at low frequencies (0.1 Hz), forming a tail related to the local corrosion process^{4,58}. However, after one week of immersion, the corrosion resistance slightly improved, which can be ascribed to the densification of the aluminium oxide/hydroxide layer; the $|Z_{10\text{ mHz}}|$ increased to $\sim 36\text{ k}\Omega\text{ cm}^2$. The tail at low frequencies disappeared, indicating that the degree of the local corrosion attack did not increase with extended immersion time.

The Bode plots of Zr-CrCC coated alloy are also shown in Fig. 3. At high and middle frequencies, the impedance and phase angle plots did not differ considerably from the non-coated sample, but a more significant difference occurred at low frequencies in the phase angle plot. After 1 h of immersion, the $|Z_{10\text{ mHz}}|$ for the Zr-CrCC-coated sample was $36\text{ k}\Omega\text{ cm}^2$ (Fig. 3a). The coated sample also showed a broader phase angle plot in the middle frequencies with a maximum phase angle of -81° at 22 Hz (Fig. 3b). More importantly, no minimum at low frequencies appeared, reflecting the protective nature of the Zr-CrCC. When extending the immersion time to

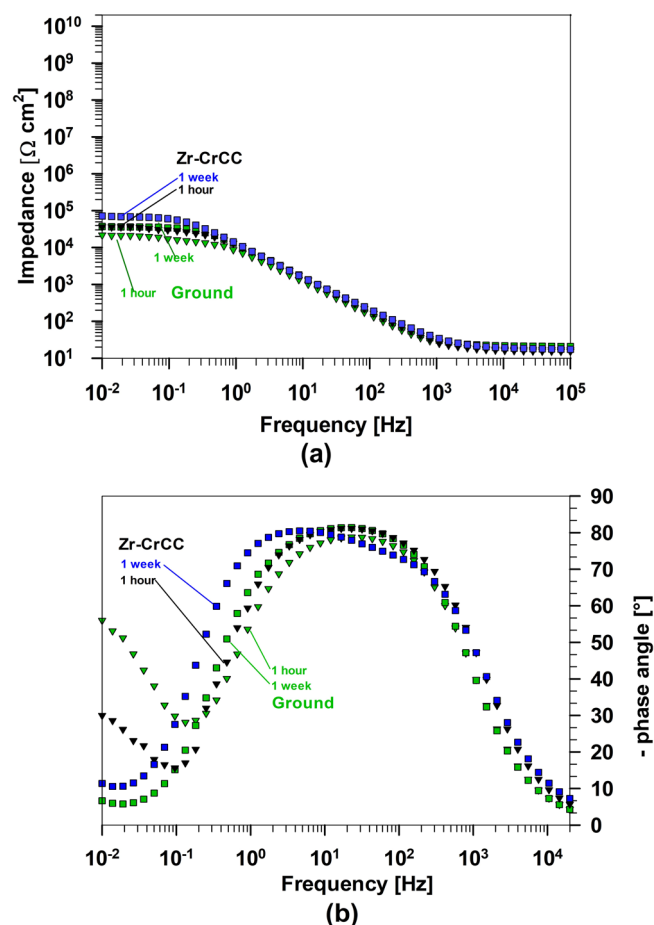


Fig. 3 | EIS results for non-coated and Zr-CrCC-coated AlSi7Mg0.3 samples. Bode plots (a) of impedance magnitude and (b) phase angle of the ground (green symbols) AlSi7Mg0.3 sample and Zr-CrCC-coated AlSi7Mg0.3, measured after immersion in 0.1 M NaCl for 1 h (triangles) and a week (squares).

one week, the corrosion protection by the Zr-CrCC was still efficient, as evidenced by the $|Z_{10 \text{ mHz}}|$ of $72 \text{ k}\Omega \text{ cm}^2$ and broadening of the frequency region where the coating shows a capacitive character.

Based on performed electrochemical measurements, it can be stated that the Zr-CrCC, despite being around 100 nanometres thick, enhanced the corrosion protection of the AlSi7Mg0.3 cast alloy in the tested corrosive medium after short (1 week) immersion.

Polyacrylic/siloxane-silica coating

The sols at various preparation steps and the final coating were detailed in our separate paper⁵¹. The polyacrylic siloxane-silica sol (abbreviated as PEHA-SS) was prepared from two separate sols (Fig. 4). Briefly, Sol 1 consists of organic precursor MAPTMS copolymerise with 2-EHA in the presence of butyl acetate (BA) and benzoyl peroxide (BPO) to start radical copolymerisation between MAPTMS and 2-EHA⁵¹. Inorganic precursor TEOS mixed with ethanol is the main component of Sol 2. The hydrolysis of TEOS was initiated by acidified water. The final hybrid sol-gel solution was obtained by combining Sol 1 and Sol 2. A detailed procedure is given in the Methods section.

The polyacrylic/siloxane-silica coating was evaluated using SEM/EDS (Fig. 5a). The surface of the coating was very smooth, without cracks or visible pores, which confirmed that the coating evenly covered the alloy surface. SEM analysis of the scribed sample showing the coating interior showed that the coating contained small, randomly arranged silicon-based domains of a few tens of nanometres in size seen as bright spots (Fig. 5b). Differences in the composition of the coating matrix and silica-rich domains

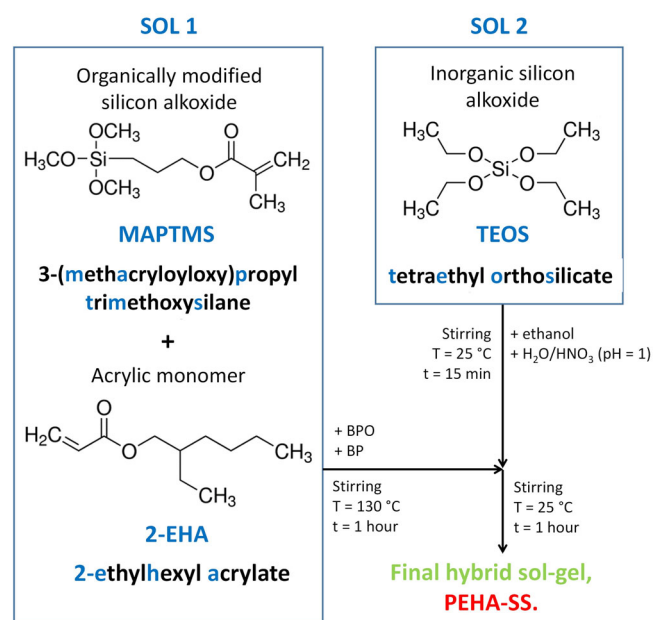


Fig. 4 | Flow chart of the polyethylhexyl acrylate siloxane-silica (PEHA-SS) preparation.

were checked by spot EDS analysis. At point x_{10} , i.e., at the bulk of the coating, the composition of the coating in weight percentage refers to Si (16.9 at.%) and O (83.1 at.%) (Fig. 5a). These are (in addition to carbon, which EDS cannot quantitatively evaluate due to the deposition of carbon layer prior the analysis), the main elements in an organosilane coating consisting of 2-EHA, MAPTMS and TEOS. Since only these two elements are in the spectrum, it can be concluded that the thickness of the coating is in the range of a few micrometres where the beam did not reach the aluminium alloy substrate. The estimated thickness of the coating along the coating cross-section is around $\sim 9 \mu\text{m}$, which is at least $90 \times$ times thicker than Zr-CrCC (Fig. 2d).

At the x_{11} site located on the nano-domain, the composition differed from point x_{10} (Fig. 5). Greater amounts of Si and O were detected at site x_{11} than at site x_{10} , i.e. Si (22.9 at.%) and O (77.1 at.%) referring to the silica (Si—O—Si) rich domain based on TEOS, as has already been noticed for similar polyacrylate siloxane-silica coatings^{51,59,60}. The presence of these domains confirmed highly condensed coating, which presents the efficient barrier corrosion protection between corrosion medium and aluminium surface^{51,59,60}.

Figure 6 a, b show SE-SEM images along the artificially made scribe of the AlSi7Mg0.3 surface coated with a PEHA-SS. The coating was removed with a sharp razor. The coating did not crack, but the peeling occurred in certain areas due to scribing, confirmed by SEM/EDS analysis, as the spectrum x_{12} had a slightly higher proportion of Si and O (coating residues). The composition of the alloy at x_{13} was identical to the ground non-coated surface (Fig. 1a).

The adhesion of the PEHA-SS coating was evaluated with an X-cross incision adhesion test (Fig. 6c, d, Supplementary Figure 3). PEHA-SS coating did not visibly peel or form flakes during the test, which confirmed that the coating adhered firmly to the surface. After deposition, the PEHA-SS coating formed a strong covalent bond Si—O—Al between Si—OH and $\text{Al}(\text{OH})_3$, which provides good adhesion to the alloy surface⁵¹. The adhesion of both coatings on the surface was assessed by designation 5B, the best assessment according to standard D3359–22⁶².

After adhesion testing, the sample surface was characterised with a confocal microscope at the site where the intersection between the incisions occurred (Fig. 6c). There were only small signs of peeling on the microscopic scale for the alloy coated with the PEHA-SS coating (Fig. 6d).

Fig. 5 | SEM images of PEHA-SS-coated AlSi7Mg0.3 samples. **a** Secondary electron (SE) and **(b)** circular backscatter detector (CBS) SEM images of the **(a)** surface of the polyacrylic/siloxane-silica-coated AlSi7Mg0.3 sample and **(b)** along an artificial scribe. The estimated coating thickness is about 9 μm . The arrow shows the silica-based domains. The x_{10} and x_{11} mark the areas where the EDS analyses were performed with the composition in atomic percentages (at.%). SEM analysis was conducted at **(a)** 0.5 kV and **(b)** 5 kV. EDS analysis was conducted at 5 kV.

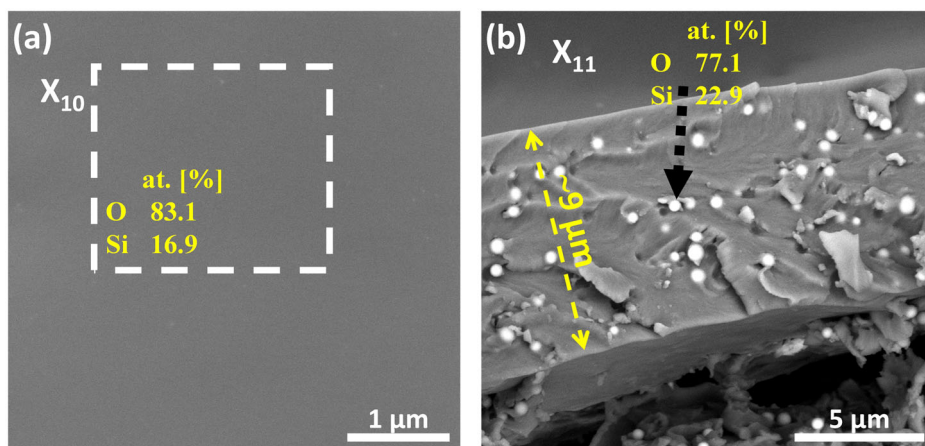


Fig. 6 | SEM images and adhesion test of PEHA-SS-coated AlSi7Mg0.3 samples. **a, b** Circular backscatter electron (CBS) SEM images of the scribe made at the polyacrylic/siloxane-silica-coated AlSi7Mg0.3 sample. The squares x_{12} and x_{13} indicate the areas where the EDS analysis was performed with the composition in atomic percentages (at.%). **c, d** Confocal microscope images after performing the cross-cut test according to the standard ASTM 3359–23⁶². SEM/EDS analyses were conducted at 5 kV.

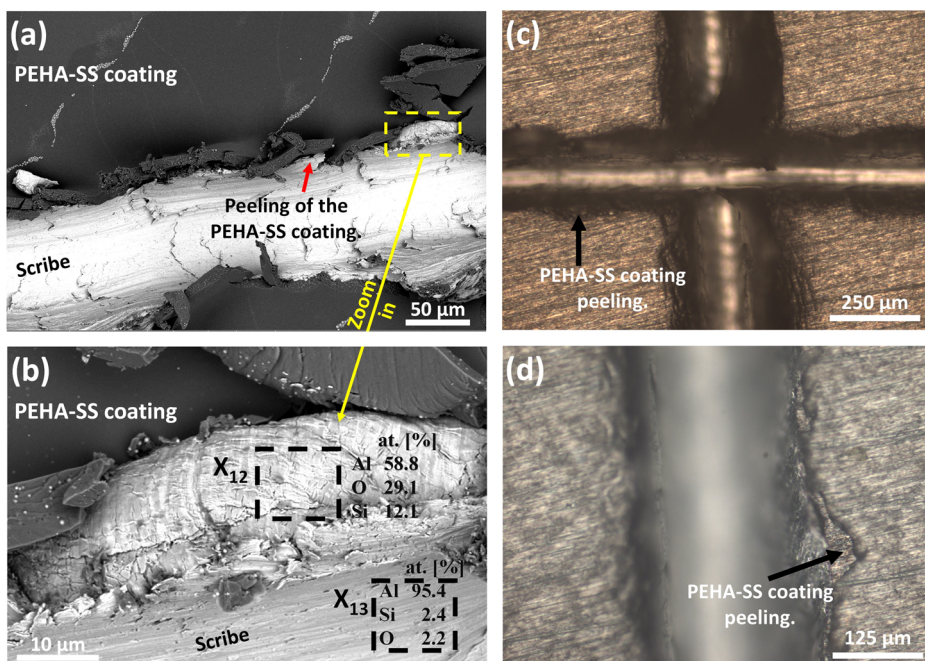


Fig. 7 | EIS results for PEHA-SS-coated AlSi7Mg0.3 samples. Bode plots of **(a)** impedance magnitude and **(b)** phase angle of AlSi7Mg0.3 coated with polyacrylic/siloxane-silica after immersion in 0.1 M NaCl for up to 4 months.

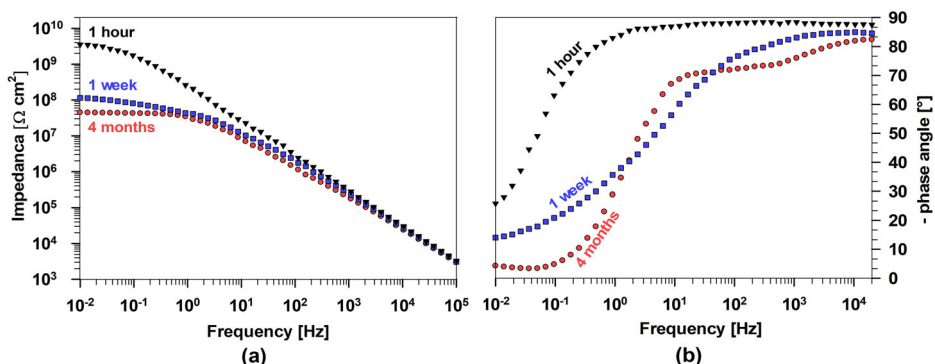
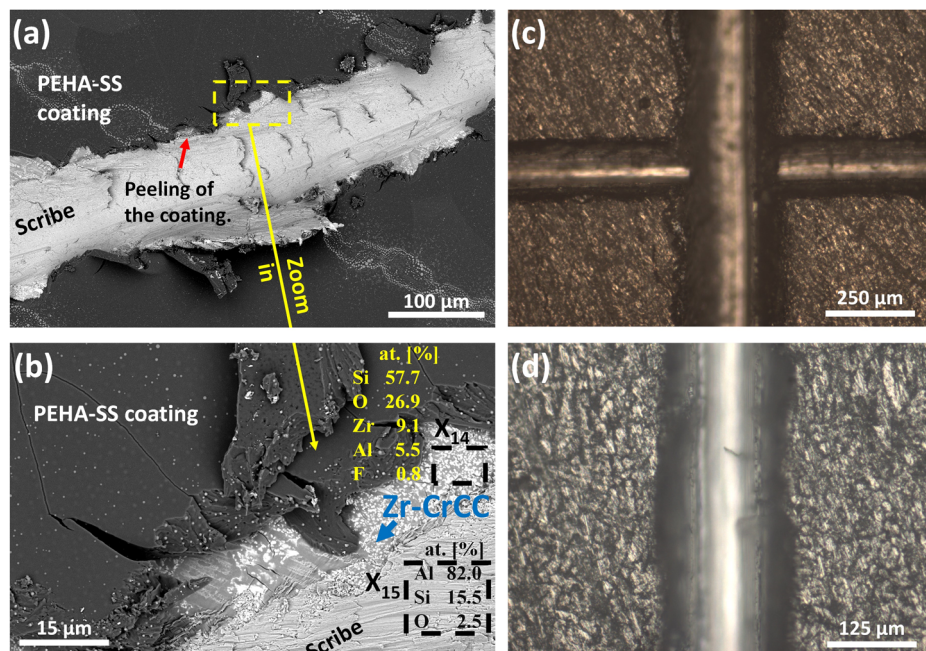


Figure 7a shows the results of electrochemical impedance spectroscopy (EIS) measurements for alloy coated with PEHA-SS as a function of frequency after 1 h, 1 week, and 4 months. In the Bode diagram, characteristics of the curves at low and medium-high frequencies record the events at the phase boundary between the coating and the substrate⁵⁹. In contrast,

measurements at high frequencies describe the behaviour of the interface between the coating and the solution after the sample is exposed to an aggressive corrosive medium.

The $|Z_{10\text{mHz}}|$ values for PEHA-SS are significantly higher (6 G Ω cm², for more than five orders of magnitude) than for the ground non-coated and

Fig. 8 | SEM images and adhesion test of Zr-CrCC+PEHA-SS-coated AlSi7Mg0.3 samples. **a, b** Circular backscatter electron (CBS) SEM images of the scribe made at the multilayer Zr-CrCC+polyacrylic/siloxane-silica-coated AlSi7Mg0.3 sample. The squares x_{14} and x_{15} indicate the areas where the EDS analysis was performed with the composition in atomic percentages (at.%). **c, d** Confocal microscope images after performing the cross-cut test according to the standard ASTM 3359. SEM/EDS analyses were conducted at 5 kV.



Zr-CrCC-coated samples (Fig. 3), confirming efficient barrier protection of the alloy surface. These values are comparable with other polyacrylate siloxane-silica coatings^{59,60,63}. The phase angle values were above -80° over a wide frequency range (over 4–5 decades in the mid- and high-frequency range), showing behaviour close to that known for a quasi-ideal capacitor (Fig. 7b). Values are related to the capability of the coating to completely blocks the entrance of a corrosive medium confirming that the preparation of hybrid PEHA-SS coating was adequate to achieve appropriate barrier protection⁵¹.

The coating was also characterised as a function of immersion time to evaluate its durability. A significant drop in impedance at the lowest frequencies of about 1.5 decades was observed after 1 week of immersion (Fig. 7a). The changes were also noticed in the phase angle plot because the values above -80° appeared in a much narrower frequency range (Fig. 7b). At longer times (4 months), the decrease was slighter. Despite the decreasing trend, the impedance value at these frequencies remained high (42 MΩ cm²). Thus, the lifespan of the coating is limited, but the impedance values remained above 1 MΩ cm², indicating durable (barrier) corrosion protection during testing time. The limited durability is probably related mainly to the swelling effect of the organic phase in contact with a corrosive medium (aqueous chloride solution).

Multilayer Zr-Cr based and polyacrylic/siloxane-silica coating

The multilayer Zr-CrCC+PEHA-SS coating was prepared by combining Zr-CrCC and PEHA-SS coatings (Supplementary Figure 1). The scribe made on this multilayer system (Fig. 8) exhibits somewhat different behaviour than observed for only PEHA-SS-coated alloy (Fig. 6). The multilayer coating did not crack (Fig. 8a). Some cracks were noted but probably caused by dehydration in low vacuum, and electron beam during SEM imaging (Fig. 8b). Again, the peeling of the coating occurred at certain spots along the scribe, but Zr-CrCC remained on the surface, observed as bright spots along the scribe (area marked with the blue arrow in Fig. 8b). The squared areas were additionally analysed with EDS. The spectrum x_{14} was recorded underneath the PEHA-SS coating with the interface with Zr-CrCC. Here, a high content of Si from the PEHA-SS was detected (57.7 at.%) along with Zr (9.1 at.%) and F (0.8 at.%) from the Zr-CrCC. Notably, Cr was not detected at 5 kV for reasons explained in the above text. The Zr-CrCC remained firmly adhered to the surface and enhanced the adhesion of the PEHA-SS coating to the substrate. The

composition of the scribe (x_{15}) refers to the underlying substrate surface (Fig. 1a).

The adhesion of the Zr-CrCC+PEHA-SS coating on the alloy surface was evaluated with an X-cross incision adhesion test (Fig. 8c, d, Supplementary Fig. 4). The coating multilayer system did not peel or form flakes, which confirms that the coatings adhered firmly to the surface. The Zr-CrCC yielded greater surface area than ground alloy due to its more rough surface (see Fig. 1a). The Zr-CrCC contains OH⁻ groups⁶⁴, which can form a strong covalent bond with the Al alloy surface (Zr–O–Al, Cr–O–Al) and at the same time with polyacrylic/siloxane-silica coating (Zr–O–Si, Cr–O–Si). Hence, increased adhesion results from more surface interactions and bonding between the pretreated alloy surface and coating due to higher surface area and the chance of bond formation. Therefore, the Zr-CrCC on the AlSi7Mg0.3 surface is a good promotor of adhesion of the sol-gel coating^{36,39}.

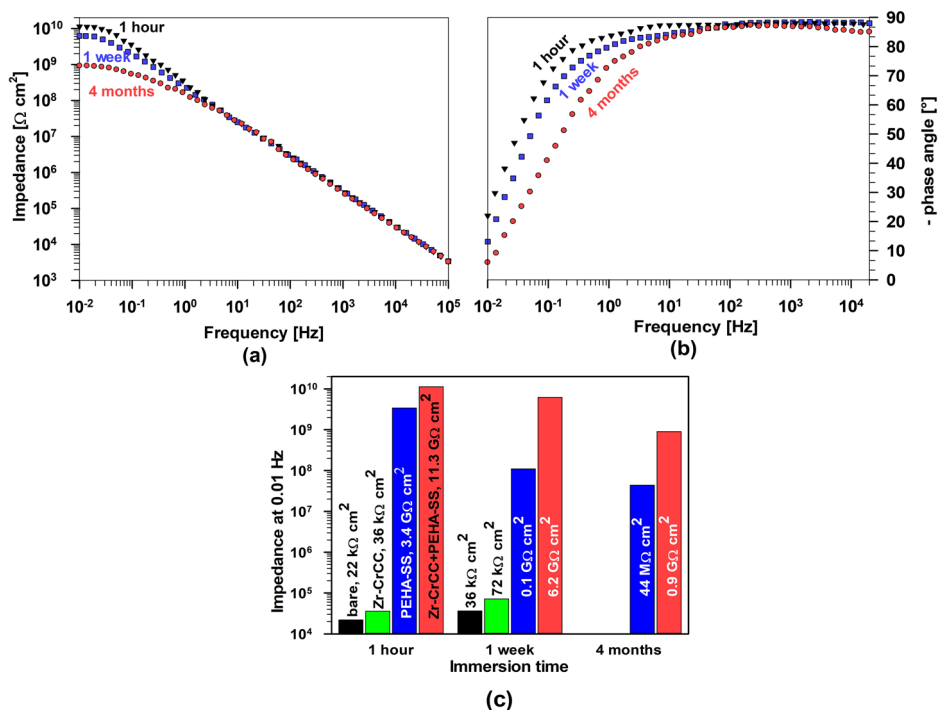
The adhesion of the multilayer coating system on the surface was assessed by designation 5B (Fig. 8c, d). Confocal microscope images showed no cracking or peeling on the microscopic scale. Some differences in the adhesion between the PEHA-SS and Zr-CrCC+PEHA-SS were observed (Fig. 6c, d, Fig. 8c, d and Supplementary Figs. 3, 4). The coating peeling along the scribe occurred only for the PEHA-SS-coated sample (Fig. 6c, d). In addition, the scribe edges were sharper for the alloy coated with ZrCC +PEHA-SS coating (Fig. 8). This can be related to the enhanced adhesion of the PEHA-SS coating to the Zr-CrCC pretreated aluminium surface.

The corrosion properties of multilayer Zr-CrCC+PEHA-SS coating were evaluated using EIS measurements as a function of immersion time. The results are presented as Bode plots (a) impedance magnitude and (b) phase angle (Fig. 9).

After 1 h of immersion, the Zr-CrCC+PEHA-SS coating exhibited an impedance magnitude value of $|Z_{10 \text{ mHz}}| = 11.3 \text{ G}\Omega \text{ cm}^2$ (Fig. 9a, c), one order of magnitude higher than PEHA-SS coating (Fig. 7a). Figure 9b shows the negative phase angle as a function of frequency. A Zr-CrCC+PEHA-SS coating has a constant phase angle of almost -90° at an even broader frequency range than PEHA-SS, reflecting the insulating properties of the multilayer coating.

EIS measurements were performed for an extended period to evaluate the corrosion protection of the polyacrylic/siloxane-silica coating and the Zr-CrCC+PEHA-SS coating (1 hour, 1 week and 4 months). At prolonged immersion, a decrease in impedance values was again noticed at lower

Fig. 9 | EIS results for Zr-CrCC+PEHA-SS-coated AlSi7Mg0.3 samples. Bode plots of (a) impedance magnitude and (b) phase angle of AlSi7Mg0.3 coated with Zr-CrCC+polyacrylic/siloxane-silica coating measured during immersion in 0.1 M NaCl for up to 4 months. c presents the impedance value at 0.01 Hz of bare AlSi7Mg0.3 sample, Zr-CrCC-coated, PEHA-SS-coated and Zr-CrCC+PEHA-SS-coated samples at selected immersion times 1 h, 1 week and 4 months).



frequencies, but the drop at low frequencies was much lower than for PEHA-SS (Figs. 7 and 9). Impedance values remained at almost 0.9 G $\Omega \text{ cm}^2$ (Fig. 9c). The durability of the coating could also be confirmed by the phase angle curves, which remained unchanged (Fig. 9b). This is related to the presence of the Zr-CrCC inner layer, which contributes an additional degree of protection and promotes the adhesion of the upper PEHA-SS coating on the surface. Their behaviour is similar to other multilayer systems on other metals consisting of conversion coating and polymer coating^{36,42,46,48,49,65–67}, despite the multilayer Zr-CrCC+PEHA-SS coating being much thinner compared to systems including polymer coatings. This result represents a good starting point for further improvements in coating deposition.

The corrosion protection of metals used for various industrial applications typically requires a salt-spray corrosion test following the standard ASTM B117. Figure 9 shows the test results after selected periods (1 day, 2 days, 4 days, and 1 week) for the uncoated sample (Fig. 10a), Zr-CrCC-coated sample (Fig. 10b), PEHA-SS-coated sample (Fig. 10c), and Zr-CrCC+PEHA-SS-coated sample (Fig. 10d). After just one day, the first corrosion products appeared on the non-coated AlSi7Mg0.3 sample (Fig. 10a). The surface colour changed from light grey to dark grey, probably related to oxidation and the formation of hydrolysed aluminium oxide layer containing some chloride (see below). White spots of corrosion products (presumably $\text{Al}(\text{OH})_2\text{Cl}$) were observed at localised sites. The amount of these corrosion products increased rapidly with the exposure time, and at the same time, the number of white spots increased. After one week, the surface was completely covered with a thick layer of corrosion products with many white dots distributed over the entire surface.

The Zr-CrCC-coated sample showed better corrosion resistance than the uncoated (Fig. 10b). In individual spots, corrosion products appeared on the surface after 2 days, while most of the surface remained protected. More corrosion products were observed after 4 days, but corrosion progressed slowly and remained localised.

The PEHA-SS-coated sample expressed more durable barrier protection during the testing period. The corrosion occurred mainly in the scribed area, where dark corrosion products were observed after 1 day (Fig. 10c). Two common compounds of a dark layer of corrosion products on the AlSi7Mg0.3 surface (magnesium-containing alloy) are magnesium hydroxide ($\text{Mg}(\text{OH})_2$) and magnesium oxide (MgO). Both of these compounds

can contribute to the darkening of surfaces over time during exposure to moisture in the air. Additionally, magnesium can form other corrosion products depending on the specific environmental conditions it is exposed to, such as (MgCO_3) or magnesium chloride (MgCl_2) when exposed to carbon dioxide or chloride ions, respectively. The amount of corrosion products then increased further after a more extended testing period.

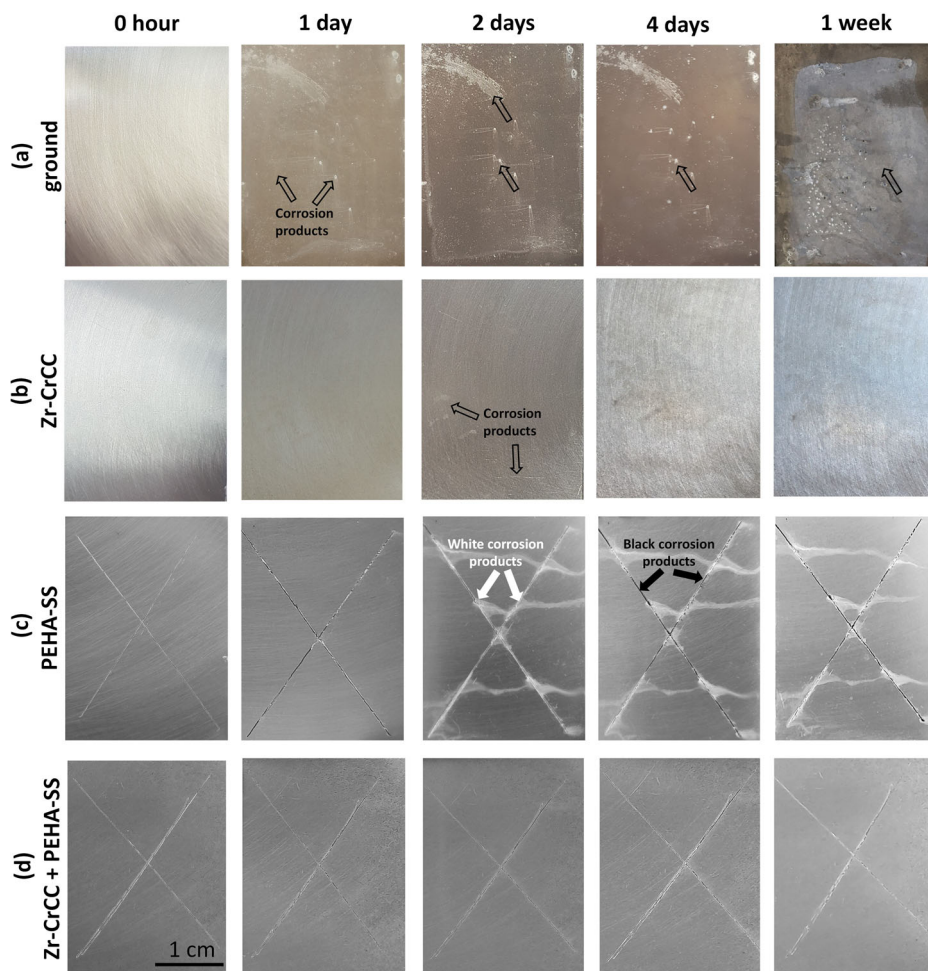
The multilayer protection (Zr-CrCC+PEHA-SS) achieved the most efficient corrosion protection. Corrosion products were only visible along with the scribe. At the same time, they were not detected on the coated area of the sample (Fig. 10d). The corrosion along the scribe was significantly reduced compared to the alloy coated with only a PEHA-SS (Fig. 10c). The Zr-CrCC thus acts as a source of complementary protection^{12,36} and, together with barrier protection ensured by the polyacrylic/siloxane-silica coating, results in long-lasting protection of the underlying substrate.

After salt spray testing for two days, the parts of the scribed areas (Supplementary Figure 5) were evaluated by SEM and point and mapping EDS analyses to assess the complementary protection of the Zr-CrCC coating.

The scribed area of the PEHA-SS-coated AlSi7Mg0.3 sample showed areas exposing the underlying substrate and areas covered by corrosion products (Fig. 11 and EDS mapping in Supplementary Fig. 6). The layer of corrosion products was relatively thick and rather voluminous, containing Al, Si, O and some Cl (S is probably the impurity from the solution) (site x_{17}). The area not covered by corrosion products (site x_{18}) contained more Al and Si originating from the substrate. Once exposed to salt spraying, the substrate within the scribe underwent selective anodic dissolution of more active metals (e.g. Mg and Al), resulting in a more voluminous corrosion product, which may redeposit at the surface. The PEHA-SS coating along the scribe (site x_{16}) showed a composition similar to that given in Fig. 8b, site x_{12} . The slight difference is due to the presence of Al and Na related to the non-soluble salts, such as aluminium oxides/hydroxides formed at the surface when exposed to a corrosive medium (NaCl).

Local corrosion attack was not observed in the scribed areas on the sample coated with Zr-CrCC+PEHA-SS coating (Fig. 12 and Supplementary Fig. 7). In contrast to the PEHA-SS-coated sample (Fig. 11), no voluminous corrosion products were observed. The scribed area (site x_{21}) showed only 6 at.% of oxygen compared to up to

Fig. 10 | Salt-spray chamber testing. The surface appearance of (a) ground AlSi7Mg0.3 sample and AlSi7Mg0.3 samples coated (b) with Zr-CrCC, (c) PEHA-SS and (d) Zr-CrCC+PEHA-SS at various exposure times in the salt-spray chamber test carried out according to standard ASTM B117. Before testing, the PEHA-SS and Zr-CrCC+PEHA-SS coated samples were scribed. The arrows mark the spots where corrosion started.



55 at.% for the PEHA-SS, sites x_{17} in Fig. 11. Furthermore, some Mg was detected, indicating that the selective dissolution of Mg was inhibited, which was not the case for the PEHA-SS-coated sample (Fig. 11). EDS maps in Supplementary Figures 6 and 7 show the difference in contents of Al and O within the scribe.

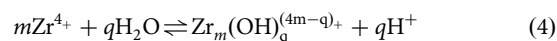
The scribed area was additionally analysed at higher magnification (x_{22} and x_{23}). No elements related to corrosion (Na, Cl) were detected. A notable finding is that in addition to substrate elements, those originating from Zr-CrCC were detected: Zr, Cr and F (area x_{22}). This means that the scribed area was recovered after exposure to salt spray by spreading the Zr-CrCC within the scribe. In addition to Zr, Cr was identified. The spreading of the Zr-CrCC by the self-release of Zr and Cr resulted in the prevention or mitigation of corrosion of the underlying substrate, as proven by the salt spray test (Fig. 10d). At the area along the scribe x_{20} , Zr, F and Cr related to Zr-CrCC coating were also detected, whereas the upper layer consisted of PEHA-SS (spot x_{19}). The presence of Cr and Zr within the scribe is evidenced by the EDS mapping (Supplementary Fig. 7).

Contribution of individual coatings to the protection mechanism of multilayer coating

The experimental observations confirmed that the multilayer Zr-CrCC + PEHA-SS deposited on AlSi7Mg0.3 was less susceptible to corrosion attack, evidenced by the absence of corrosion products in the scribed area. Evidence also showed that the Zr-CrCC contributed to active corrosion protection since the elements originating from the conversion coating (Zr, Cr) were identified within the scribe. This process supposedly involves the release of Zr and Cr species and their transfer

and formation of related (hydro)oxides at the sites within the scribe. Although the exact mechanism cannot be postulated based solely on the results presented in this study, some premises can be proposed, supported by the literature data on similar systems. The protection mechanisms of the scribed PEHA-SS and Zr-CrCC+PEHA-SS coatings are schematically proposed in Fig. 13.

During Zr-CrCC coating formation in an acidic conversion bath ($\text{pH} \approx 3.9$), less noble metals such as Mg and Al are dissolved, additionally supported by the action of fluoride ions to attack the thin native oxide layer, thus facilitating access of ZrF_6^{2-} species to the metal substrate (reaction 2). In the absence of F-containing species in the solution, the favourable reaction is the formation of Zr hydroxide through the chemical reaction of hydrolysis³⁴:



The role of fluoride in the conversion baths is dual: (i) thinning of the oxide layer formed spontaneously on the metal surface and (ii) shift the pH at which Zr hydroxide precipitates to higher pH values (between 3 and 6 depending on the concentration of Zr species) due to the formation of stable ZrF_q^{4-q} complexes³⁴; the increase of precipitation pH has an important practical meaning since it is beneficial for aluminium substrate tending to corrode at acidic pH^{12,30,34}.

The concomitant cathodic reaction (1) of oxygen reduction provides the conditions for the deposition of Zr and Cr (hydr)oxides formed through reactions (2) and (3) once the pH reaches values around 4³⁴. The Zr-CrCC layer, around 100 nanometres thick (Fig. 2), acts as a first line of defence, preventing further oxidation of the alloy in

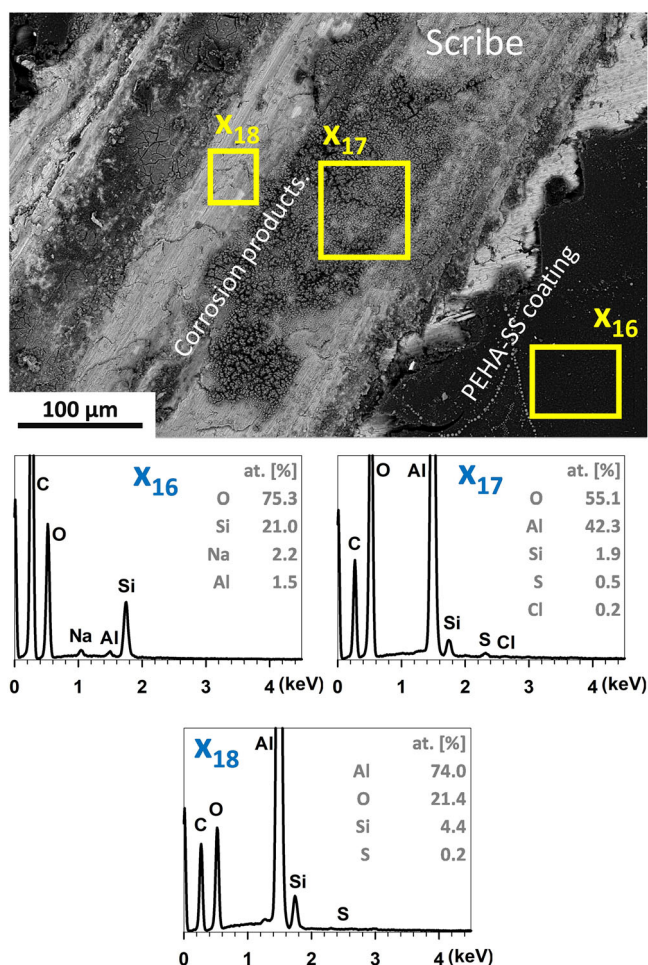


Fig. 11 | Circular backscatter electron (CBS) SEM image of the scribe made at the polyacrylic/siloxane-silica-coated AlSi7Mg0.3 sample taken after two days of exposure in the salt spray chamber. The squares x_{16} , x_{17} , and x_{18} indicate the area where the EDS analysis was performed with compositions in atomic percentages (at.%). SEM/EDS analyses were conducted at 10 kV.

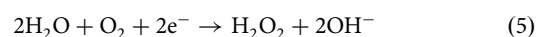
a corrosive medium for the first days of testing (Fig. 10b). Similar Zr/Cr-containing coatings were investigated in the literature. Li et al. reported that the Alodine® T5900 (Henkel) comprised a biphasic structure of hydrated zirconia ($\text{ZrO}_2 \cdot 2\text{H}_2\text{O}$) mixed with Cr(III) (hydr)oxides ($\text{Cr}(\text{OH})_3$, CrOOH and Cr_2O_3) precipitated above the fluoroaluminate interlayer on AA2024^{68,69}. The distribution of Cr was not uniform throughout the coating but was elevated around the pits. The coating provided both anodic and cathodic protection by physically blocking Al-rich sites and Cu-rich IMPs⁶⁸. Guo and Frenkel found that the Cr content in the Alodine® T5900 (Henkel) coating was only one-fourth of the Zr content. The coating thickness was 40–120 nm, considerably thicker than the conversion coating without Cr species⁷⁰. Qi et al. reported^{17,18} that SurTec® ST650 (SurTec) contained ZrO_2 , ZrF_4 , $\text{Cr}(\text{OH})_3$, $\text{Cr}_2(\text{SO}_4)_3$, CrF_3 , CrO_3 , and CrO_4^{2-} , similar to our previous study²⁴.

Nine micrometres thick PEHA-SS sol-gel forms a smooth, uniform coating that acts as a barrier to the dissolution of the underlying substrate (Fig. 7). However, the locally damaged, scribed PEHA-SS surface represents the starting point for the exposure of underlying AlSi7Mg0.3 substrate to the corrosive environment (Fig. 10c), schematically presented in Fig. 13c. As a result, the aluminium and magnesium ions are dissolved, forming corrosion products consisting mainly of hydrated aluminium oxide containing chloride ($\text{Al}(\text{OH})_2\text{Cl}$). Due to the absence of any active protection, the area freely corrodes in the corrosion medium (Fig. 13c).

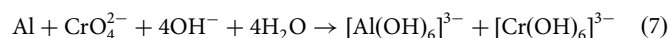
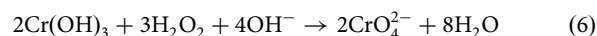
A multilayer coating system (Fig. 13b) consisting of a thin Zr-CrCC and micrometre-thick hybrid sol-gel (PEHA-SS) coating provides (i) less coating peeling and (ii) durable active corrosion protection once damaged (Fig. 13d, f). These experimental findings can be substantiated as follows.

(i) Due to the presence of Zr-CrCC, better adhesion of PEHA-SS to the alloy surface is achieved, resulting in less peeling along the scribe (Fig. 8). PEHA-SS coating offers a dense polymerised Si–O–Si structure (Fig. 13e) due to the combined benefits of organic and inorganic components. With a Zr-CrCC as an interlayer, strong covalent bonds Al–O–Zr, Al–O–Cr, Cr–O–Si, and Zr–O–Si are formed^{34,36}, and the coating firmly adhering to the alloy surface, preventing the coating from peeling (Figs. 8, 10d, 12). The beneficial effect on the conversion coating as an interlayer between the substrate and outer organic-based coating are in line with the results published for similar systems^{36,38,43,48}.

(ii) Zr-CrCC redeposition at the scribed surface acts as an active inhibition and repassivates the damaged area along the scribe (Fig. 12). In fact, the ability of active inhibition of conversion coatings containing trivalent chromium was already reported⁷⁰ and connected to the possibility of transient formation of Cr(VI) species during more extended immersion in the electrolyte, as shown by Raman spectroscopy^{68,69}. The latter process would be enabled by the locally produced H_2O_2 as a product of oxygen reduction at the cathodic sites according to:

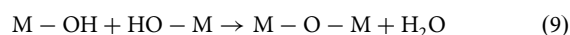
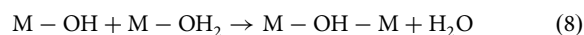


Hydrogen peroxide would then act as an oxidation agent for Cr(III) species⁶⁹ through reaction (6); chromate species formed are then reduced, resulting in the formation of passivating Cr(III) hydroxide through reaction (7):



It was proposed that Cr(VI) species are mobile and thus be involved in repairing damaged sites⁶⁹, similar to the mechanism of chromate conversion coatings but with a much smaller concentration of Cr(VI) species. Using the artificial scratch cell⁷⁰, Guo and Frankel proved that Cr species, in contrast to Zr, were detected in the exposed electrolyte and could thus be released and transferred to distant sites. As shown by XPS, the amount of Cr(VI) species is small, i.e. less than 3% of the total chromium¹⁷ and 0.1 to 1% of the coating weight¹⁸.

Whether the transient formation of Cr(VI) species is responsible for the active protection by Zr-CrCC observed in this study cannot be stated since speciation is impossible using only EDS. In our previous study on SurTec® ST650 coating, XPS could not identify chromate species unambiguously due to the overlapping with CrF_3 peaks²⁴. If present, their concentration would be minimal. However, the results presented in this study prove that the active corrosion protection mechanism is operative. Another possible mechanism, not necessarily involving the formation of chromate species, can be suggested. Namely, the Zr-CrCC can be regarded as condensed sol going through ololation (reaction 8) and oxolation (reaction 9), resulting in polymerisation accompanied by the release of water molecules³⁴:



where M is Zr or Cr (Fig. 13f). Both Zr and Cr belong to classes of elements which form polycations involved in the condensation of metal complexes in solution, in which the cations are linked by hydroxo (HO^-) or oxo (O^{2-}) bridges. The condensation is initiated by hydroxylation⁷¹.



Fig. 12 | Circular backscatter electron (CBS) SEM images of the scribe made at the Zr-CrCC+poly-acrylic/siloxane-silica-coated AlSi7Mg0.3 sample taken after two days of exposure in the salt spray chamber. The squares x_{19} – x_{23} indicate the area where the EDS analysis was performed with compositions in atomic percentages (at.%). SEM/EDS analyses were conducted at 10 kV.

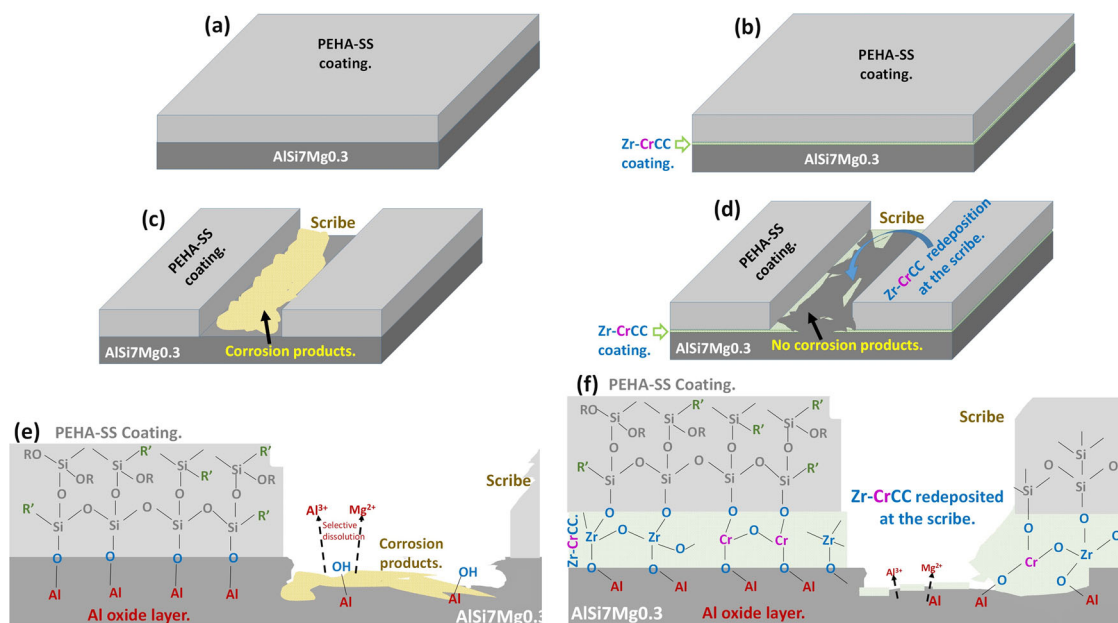
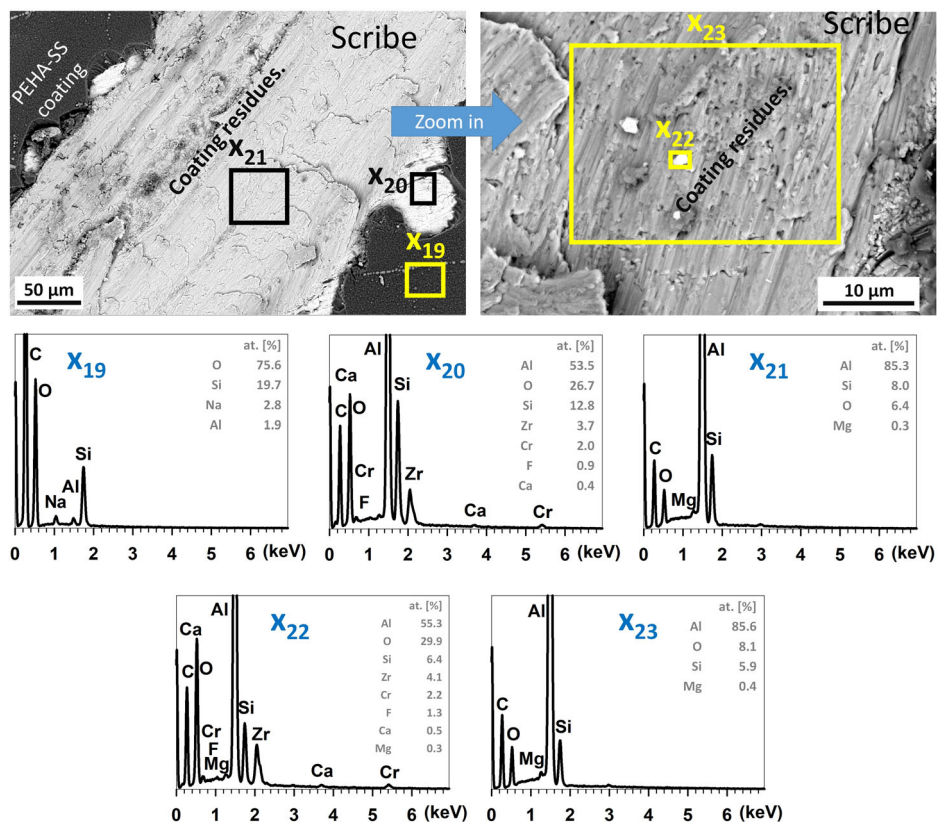
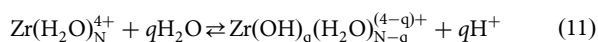


Fig. 13 | **a, b** The schematic presentation of the as-prepared PEHA-SS coating and Zr-CrCC+PEHA-SS coating deposited on the Al-Si7-Mg0.3 surface. **c, d** Schematic presentation of the corrosion along the scribe of the PEHA-SS-coated sample and Zr-CrCC+PEHA-SS-coated sample after prolonged exposure in the salt spray chamber. While the scribe on the PEHA-SS coating was filled with corrosion products, the Zr-CrCC coating redeposited within the scribe, and no corrosion attack was observed. **e** Schematic presentation of the chemical composition of the PEHA-SS and the interface with the substrate showing the formation of

the corrosion products within the scribe. **f** Schematic presentation of the Zr-CrCC + PEHA-SS multilayer chemical composition and interface with the substrate showing the mechanism of enhanced adhesion, redeposition of Zr-CrCC and consequent repassivation along the scribed area. For the sake of simplicity, the heterogeneity of the substrate comprising matrix with eutectic phase with IMPs was not considered here since it was already described in section Deposition and characterisation of Zr-Cr conversion coating.

In the case of Zr, a general hydrolysis model for mononuclear and polynuclear Zr-species can be presented as reaction (11)⁷¹:



Tetrameric species, $\text{Zr}_4(\text{OH})_8^{8+}$ or more precisely $[\text{Zr}_4(\text{OH})_8(\text{OH}_2)_{16}]^{8+}$, were shown to be the main building block of ZrCC^{34,72}. In the case of Cr, dimer $[\text{Cr}_2(\text{OH})_2(\text{OH}_2)_8]^{4+}$, trimer $[\text{Cr}_3(\text{OH})_4(\text{OH}_2)_9]^{5+}$ and tetramer $[\text{Cr}_4(\text{OH})_6(\text{OH}_2)_{10}]^{6+}$ may form among which is the trimer stable and most chemically inert of all Cr polycations⁷¹. The distribution, however, depends on the Cr species concentration and pH⁷¹. Entities of polycations are linked by $[\text{H}_3\text{O}_2]^-$ double bridges ligands. Since the Cr polycations are inert towards ligand substitution, the structure, by ageing, is transformed into characteristic amorphous chromium gels and oxyhydroxide. It has already been proposed that the formation of chromate conversion coatings is consistent with sol-gel chemistry principles⁷³, so similar consideration of hydrolysis and condensation may also be viable for trivalent chromium coatings without necessarily forming chromate species^{17,74}.

The released water molecules, reactions (8) and (9), facilitate the diffusion of Zr and also Cr species within the coating, filling the gaps and defects in the damaged regions caused by the dissolution of aluminium exposed to the chloride medium (Fig. 13f). Zr and Cr species react with atmospheric oxygen and moisture to form a new layer of Zr/Cr hydroxide, effectively sealing the damaged region. Further polymerisation of the Zr and Cr species results in forming new bonds and creating a network of $\text{Zr}-\text{O}-\text{Zr}$ ^{34,61} and $\text{Cr}-\text{O}-\text{Cr}$ ^{57,74,75}, which gradually regenerates the Zr/Cr-based protective layer, effectively healing the damaged region^{23,29} (Fig. 13f). This regeneration can occur over a certain period, and the coating can regain its protective properties. The mechanism of active corrosion prevention along the scribe can be thus explained as a combination of chemical reactions and physical processes (Fig. 13f). These findings are consistent with previous studies of self-healing coatings^{23,69,70,73,76} and were confirmed with EDS analysis along the scribe (e.g., during salt spray testing) presented in Figs. 8, 10, 12 and Supplementary Fig. 7.

Overall, the active properties of Zr-CrCC contribute to the long-term, four-months long corrosion protection of multilayer Zr-CrCC+PEHA-SS by continuously repairing and maintaining the integrity of the coating, thus prolonging the service life of the coated aluminium alloy. It is noteworthy, however, that the active corrosion properties of Zr-CrCC are generally effective for minor damages, such as a scribe or other small defects. Severe or extensive damage may exceed the self-healing capabilities of the coating.

Table 2 | AlSi7Mg0.3 (ENAC 42100) alloy composition certified by the producer

Element	Fe	Si	Mn	Ti	Cu	Mg	Zn
Weight percentage (%)	0.15	6.5–7.5	0.10	0.18	0.03	0.30–0.45	0.07

The specific rate and effectiveness of self-healing can vary depending on factors such as the coating formulation, environmental conditions, and the extent of damage.

In summary, this study showed that the two modes of corrosion protection of AlSi7Mg0.3 using hexafluoro-zirconated trivalent chromium coating Zr-CrCC (as primary active corrosion protection) and polyacrylic/siloxane-silica coating PEHA-SS (as barrier protection) achieved a complementary effect when deposited as a multilayer system. Albeit differing in thickness, morphology and composition, individual layers achieved synergy when used as a multilayer. The novelty of the study lies in developing the multilayer corrosion protection comprising a thin Zr-CrCC and several micrometres thick sol-gel coatings, in contrast to commonly used organic coatings several tens of micrometres thick. Further, the majority of previous studies have been performed on wrought Al alloys; the possibility to effectively protect cast Al alloys is of importance to their increasing use in industry due to their economic advantages in terms of shorter processing cycles and assembly costs. These promising results offer an insight into the interfacial process of the multilayer and represent a good basis for further studies focusing on combining several types of coatings to achieve the optimal multilayer system mutually supplying each other advantageous properties. It was postulated that the sol-gel nature of zirconium and chromium oxyhydroxides is related to the self-healing ability of Zr-Cr conversion coatings.

Methods

Metal substrate

The study was performed on the aluminium alloy AlSi7Mg0.3 (EN AC-42100) distributed by Talum d. d., Slovenia. The alloy composition is given in weight percentage in Table 2.

The bulk plate was cut into cuboids sized 6 cm × 4 cm × 1 cm. The sample surface was ground with a LaboPol-6 grinding machine (Struers) with SiC emery papers of grades 320, 500, 800, 1000, 1200, and 2400 distributed by Struers. Grinding was carried out in tap water to remove grinding residues and prevent local overheating of the material. The process was carried out until the oxide layer and other impurities were removed from the surface to obtain an evenly ground surface. After grinding, the samples were rinsed with deionised water, followed by a two-minute cleaning by immersion in ethanol (99%, Carlo Erba) in an ultrasonic bath.

Coating deposition

Ground metal samples were subject to the three-step process: degreasing with alkaline cleaner, acid desmutting and passivation (Table 3). Commercial reagents supplied by SurTec® (SurTec International GmbH) were used; their concentrations and related parameters (immersion times and bath temperatures), as recommended by the producer, are summarised in Table 3. Following standard procedure, the degreasing, desmutting and formation of conversion coating (passivation) were performed in a 250-mL polyethylene cup.

Table 3 | The three-step process of deposition of Zr-CrCC using SurTec® procedure (including rinsing with deionised water of room temperature between each step) with appropriate reagents, their concentrations, defined immersion times and bath temperatures given by the producer

Steps	Reagents	Concentrations (vol. %)	Immersion time (min)	Temperature (°C)
1. step – degreasing, pH=8.3	ST061 and ST089	5% and 0.5%	10	50
rinsing	deionised water		1	
2. step – desmutting, pH=1.5	ST496	20 %	5	23
rinsing	deionised water		1	
3. step – passivation, pH=3.9	ST650	20 %	5	35
rinsing	deionised water		1	

Passivation denotes the deposition of the Zr-CrCC using ST650 reagent.

ST061® is multi-metal degreasing for light metals, SurTec® ST089 is a recyclable soak detergent SurTec® 089 contains non-ionic surfactant alcohols such as amines, coco alkyl, and ethoxylated fatty alcohol. SurTec® ST496 is a standard desmutter for aerospace, electronics, and automotive applications, applicable for desmutting Si-, Zn-, and Cu- containing aluminium alloys. SurTec® ST650, a hexafluoro-zirconate conversion bath with trivalent chromium Cr(III), was used to prepare the final coating according to the conditions in Table 2. The commercial conversion coating SurTec® ST650 in the text was denoted as Zr-CrCC.

For SEM analysis of the microstructure (Fig. 1b), non-coated AlSi7Mg0.7 samples were water-ground successively using SiC-paper up to 4000 grit and then diamond-polished using polishing cloth (MD-Nap, Struers), non-water polishing using 1 µm diamond paste (DP-Paste P, Struers) and alcohol-based lubricant (DP-Lubricant Blue, Struers).

The polyacrylic/siloxane-silica (hybrid sol-gel) sols were synthesised from⁵¹: acrylate monomer 2-ethylhexyl acrylate (2-EHA; > 99%, Sigma-Aldrich), initiator benzoyl peroxide (BPO, > 99%, Aldrich), solvent butyl acetate (BA; > 99%, Sigma-Aldrich), the organically modified precursor [3-(methacryloyloxy)propyl]trimethoxysilane (also known as 3-(trimethoxysilyl)propyl methacrylate or silane A174) (MAPTMS, > 98%, Sigma-Aldrich), and the inorganic precursor tetraethyl orthosilicate (TEOS, 99.9%, Aldrich), HNO₃ (> 70%, Sigma-Aldrich), deionised water prepared with a Milli-Q direct instrument, with an electrical resistivity of water of 18.2 MΩ cm at 25 °C (Millipore) and anhydrous ethanol (99%, Carlo Erba).

The synthesis steps of the sol-gel are shown in Fig. 4. Sol 1 was prepared from 0.128 g of BPO, 14 mL of BA, 1.888 mL of MAPTMS and 10.5 mL of 2-EHA while stirring. The reaction mixture (Sol 1) was heated at reflux (at ~ 130 °C) for one hour. In the meantime, the inorganic sol was prepared (Sol 2) from 4.2 mL of TEOS in a 25 mL reactor and 9.3 mL of ethanol. The flask was placed on a magnetic stirrer, and 0.7 mL of H₂O/HNO₃ solution (pH 1.0) was added dropwise with constant stirring. The mixture was then stirred for 15 minutes at room temperature. After 1 h of refluxing Sol 1, the reaction mixture was cooled to ambient temperature. Then, the prepared Sol 2 was added dropwise at constant stirring in Sol 1. After combining, the mixture was stirred for another hour at room temperature.

The prepared polyacrylic/siloxane-silica coating was applied to the pre-prepared surface of the alloys by dipping method with a dip-coater RDC 15 (Bungard). The one-step deposition of the coating was performed with a dip- and pull-rate speed of 14 cm/min. The sample was immersed in the sol for 3 s. The deposited coatings on alloys were thermally cured in the oven, where the temperature was slowly increased (heating rate 5 °C/min) to a final temperature of 180 °C. The curing lasted 1 h.

Surface and coating characterisation

The morphology of the ground alloy AlSi7Mg0.3 samples and samples coated with Zr-CrCC, PEHA-SS and Zr-CrCC+PEHA-SS was analysed with a field emission electron microscope (FESEM) FEI Helios Nanolab 650 Dual beam associated with energy dispersive X-ray spectrometer (EDS) Oxford Instruments X-max SDD (50 mm²), using Aztec software. Before analysis, the sol-gel coatings were scribed with a diamond tip; the thickness of the coating was determined at the scribe. The samples were coated with a thin carbon layer with BAL-TEC SCD 005. Samples' surface imaging was performed with secondary electrons (SE) and a circular backscatter detector (CBS) at acceleration voltages of 0.5 kV, 2 kV, 5 kV, 10 kV or 15 kV. The chemical composition of the selected areas on the surface was analysed using EDS at 5 and 10 kV in point and mapping modes.

The cross-hatch tester kit (brand Cgoldenwall) was used to test the adhesion of AlSi7Mg0.3 samples coated with PEHA-SS and Zr-CrCC+PEHA-SS. Coatings were cross-hatched with the specified tool (diamond razors) to produce a net-patterned surface (Supplementary Fig. 4a). Finally, the patterned surface was covered with # 810 ScotchMagic™ tape, which was pressed firmly against the surface and slowly peeled off. Based on the fragments removed from the coating, the degree of adhesion was assessed according to ASTM standard D3359-23 (ISO-2409)⁶² on a scale from 0B to

5B. After the adhesion test, the selected crossed area was additionally characterised with the confocal microscope at 10× and 20× magnification (Axio, CSM 700, Zeiss, Göttingen, Germany and Axio CSM 700 3D software).

Electrochemical measurements were performed in a three-electrode system in a 250 mL corrosion cell at room temperature. The samples were fixed to the cell with a holder, and the exposed sample surface (1 cm²) served as the working electrode. The reference electrode was a saturated silver/silver chloride electrode (Ag/AgCl) with $E = 0.197$ V vs. standard hydrogen electrode, and a graphite rod with a diameter of 5 mm acted as a counter electrode.

Measurements were performed with a potentiostat/galvanostat Autolab 204 M (Metrohm Autolab) with Nova 2.1 software to control the measurement and analyse the obtained data. A corrosive medium solution (0.1 M NaCl) was prepared using sodium chloride (> 99.5%, Fisher) and deionised water (Milli-Q Direct).

Electrochemical impedance spectroscopy was performed in the frequency range between 10 mHz and 100 kHz. For ground and ZrCC-coated samples, the EIS measurements were conducted after 1 h of immersion in 0.1 M NaCl. For the samples coated with PEHA-SS and Zr-CrCC+PEHA-SS coatings, measurements were also performed after 1 week and 4 months of immersion in the tested medium. The measurements were performed at least in triplicate, and the representative one was presented in graphs.

The corrosion testing in a salt-spray chamber was conducted according to the international standard ASTM B117⁷⁷. The test was performed in a controlled atmosphere in a chamber with a volume of 0.17 m³ (ASCOTT). NaCl solution ($\gamma = 58.5$ g/L) was pumped into the chamber through the filter columns. The temperature in the chamber was 35 °C ± 2 °C.

Before testing, the edges of the samples were protected with adhesive tape to minimise the corrosion of unprotected parts. The X-cross was made with a sharp diamond cutter on the sample coated with the PEHA-SS coating. The samples were placed into a plastic holder at an angle of 45°. The sample surface was photographed at the selected time up to 168 h (7 days). After 2 days of exposure, the samples were also analysed along with the scribe using SEM/EDS.

Data availability

The data that support the findings of this study are available from the corresponding author upon reasonable request.

Received: 21 October 2023; Accepted: 19 April 2024;

Published online: 28 May 2024

References

- Berlanga-Labari, C., Biezma-Moraleda, M. V. & Rivero, P. J. Corrosion of Cast Aluminum Alloys: A Review. *Metals* **10**, 1384 (2020).
- Davis, J. R. *Corrosion of Aluminum and Aluminum Alloys*. (ASM International, Novelty, Ohio, The United States of America, 1999).
- Kuchariková, L., Liptáková, T., Tillová, E., Kajánek, D. & Schmidová, E. Role of Chemical Composition in Corrosion of Aluminum Alloys. *Metals* **8**, 581 (2018).
- Milošev, I. et al. Mechanism of Corrosion of Cast Aluminum-Silicon Alloys in Seawater. Part 1: Characterization and Field Testing of Bare Alloys in the Adriatic Sea. *Corrosion* **79**, 193–212 (2022).
- Zhao, J. et al. Effects of chromate and chromate conversion coatings on corrosion of aluminum alloy 2024-T3. *Surf. Coat. Technol.* **140**, 51–57 (2001).
- Kendig, M. W. & Buchheit, R. G. Corrosion Inhibition of Aluminum and Aluminum Alloys by Soluble Chromates, Chromate Coatings, and Chromate-Free Coatings. *Corrosion* **59**, 379–400 (2003).
- Gharbi, O., Thomas, S., Smith, C. & Birbilis, N. Chromate replacement: what does the future hold? *Npj Mater. Degrad.* **12**, 1–8 (2018).
- Becker, M. Chromate-free chemical conversion coatings for aluminum alloys. *Corros. Rev.* **37**, 321–342 (2019).

9. Santa Coloma, P. et al. Chromium-free conversion coatings based on inorganic salts (Zr/Ti/Mn/Mo) for aluminum alloys used in aircraft applications. *Appl. Surf. Sci.* **345**, 24–35 (2015).
10. Chauhan, L. R. et al. Development of eco-friendly chemical conversion coating for aluminium substrate. *J. Indian Chem. Soc.* **99**, 100392 (2022).
11. Cristoforetti, A., Fedel, M., Deflorian, F. & Rossi, S. Influence of deposition parameters on the behavior of nitro-cobalt-based and Ti-hexafluoride-based pretreatments. *J. Coat. Technol. Res.* **19**, 859–873 (2022).
12. Milošev, I. & Frankel, G. S. Review—Conversion Coatings Based on Zirconium and/or Titanium. *J. Electrochem. Soc.* **165**, C127–C144 (2018).
13. Dabalà, M., Armelao, L., Buchberger, A. & Calliari, I. Cerium-based conversion layers on aluminum alloys. *Appl. Surf. Sci.* **172**, 312–322 (2001).
14. Sainis, S. & Zanella, C. A Study of the Localized Ceria Coating Deposition on Fe-Rich Intermetallics in an AlSiFe Cast Alloy. *Materials* **14**, 3058 (2021).
15. Harvey, T. G. Cerium-based conversion coatings on aluminium alloys: a process review. *Corros. Eng. Sci. Technol.* **48**, 248–269 (2013).
16. Rodič, P., Milošev, I. & Frankel, G. S. Corrosion of Synthetic Intermetallic Compounds and AA7075-T6 in Dilute Harrison's Solution and Inhibition by Cerium(III) Salts. *J. Electrochem. Soc.* **170**, 031503 (2023).
17. Qi, J.-T. et al. Trivalent chromium conversion coating formation on aluminium. *Surf. Coat. Technol.* **280**, 317–329 (2015).
18. Qi, J. et al. Influence of pre- and post-treatments on formation of a trivalent chromium conversion coating on AA2024 alloy. *Thin Solid Films* **616**, 270–278 (2016).
19. Qi, J., Świątowska, J., Skeldon, P. & Marcus, P. Chromium valence change in trivalent chromium conversion coatings on aluminium deposited under applied potentials. *Corros. Sci.* **167**, 108482 (2020).
20. Li, L., Doran, K. P. & Swain, G. M. Electrochemical Characterization of Trivalent Chromium Process (TCP) Coatings on Aluminum Alloys 6061 and 7075. *J. Electrochem. Soc.* **160**, C396 (2013).
21. George, F. O., Skeldon, P. & Thompson, G. E. Formation of zirconium-based conversion coatings on aluminium and Al–Cu alloys. *Corros. Sci.* **65**, 231–237 (2012).
22. Golru, S. S., Attar, M. M. & Ramezanzadeh, B. Morphological analysis and corrosion performance of zirconium based conversion coating on the aluminum alloy 1050. *J. Ind. Eng. Chem.* **24**, 233–244 (2015).
23. Yoganandan, G., Pradeep Premkumar, K. & Balaraju, J. N. Evaluation of corrosion resistance and self-healing behavior of zirconium–cerium conversion coating developed on AA2024 alloy. *Surf. Coat. Technol.* **270**, 249–258 (2015).
24. Mujdrica Kim, M., Kapun, B., Tiringier, U., Šekularac, G. & Milošev, I. Protection of Aluminum Alloy 3003 in Sodium Chloride and Simulated Acid Rain Solutions by Commercial Conversion Coatings Containing Zr and Cr. *Coatings* **9**, 563 (2019).
25. Šekularac, G., Kovač, J. & Milošev, I. Prolonged protection, by zirconium conversion coatings, of AlSi7Mg0.3 aluminium alloy in chloride solution. *Corros. Sci.* **169**, 108615 (2020).
26. Zhou, P. et al. Critical role of pretreatment on the corrosion resistance of Zr conversion coating on 6061 aluminum alloy: The combined effect of surface topography and potential difference between different phases. *Surf. Coat. Technol.* **377**, 124904 (2019).
27. Liu, X. et al. Environmentally Friendly Zr-Based Conversion Nanocoatings for Corrosion Inhibition of Metal Surfaces Evaluated by Multimodal X-ray Analysis. *ACS Appl. Nano Mater.* **2**, 1920–1929 (2019).
28. Nabizadeh, M. et al. Unraveling the formation mechanism of hybrid Zr conversion coating on advanced high strength stainless steels. *Surf. Coat. Technol.* **441**, 128567 (2022).
29. Zhan, W. et al. Preparation and Characterization of Synchronous Chemical Conversion Coating on 6061 Aluminum Alloy/7075 Aluminum Alloy/Galvanized Steel Substrates. *Metals* **12**, 2011 (2022).
30. Samaei, A. & Chaudhuri, S. Role of zirconium conversion coating in corrosion performance of aluminum alloys: An integrated first-principles and multiphysics modeling approach. *Electrochim. Acta* **433**, 141195 (2022).
31. Fockaert, L. I. et al. Effect of organic additives in fluoacid-based Ti and Zr-treatments for galvanized steel on the stability of a polymer coated interface. *Prog. Org. Coat.* **146**, 105738 (2020).
32. Cerezo, J. et al. The effect of surface pre-conditioning treatments on the local composition of Zr-based conversion coatings formed on aluminium alloys. *Appl. Surf. Sci.* **366**, 339–347 (2016).
33. Shen, G.-T., Chen, S.-Y., Huang, C.-Y. & Lin, C.-S. Microstructural evolution and corrosion behavior of constituent particles of AA2024-T3 Al alloy during zirconium conversion coating. *Appl. Surf. Sci.* **635**, 157657 (2023).
34. Kraš, A. & Milošev, I. The Aqueous Chemistry of Zirconium as a Basis for Better Understanding the Formation of Zirconium Conversion Coatings: Updated Thermodynamic Data. *J. Electrochem. Soc.* **170**, 021508 (2023).
35. Pourbaix, M. *Atlas of Electrochemical Equilibria in Aqueous Solutions*. (National Association of Corrosion Engineers, 1974).
36. Asemani, H. R., Ahmadi, P., Sarabi, A. A. & Eivaz Mohammadloo, H. Effect of zirconium conversion coating: Adhesion and anti-corrosion properties of epoxy organic coating containing zinc aluminum polyphosphate (ZAPP) pigment on carbon mild steel. *Prog. Org. Coat.* **94**, 18–27 (2016).
37. Moreira, V. B., Meneguzzi, A., Jiménez-Piqué, E., Alemán, C. & Armelin, E. Aluminum Protection by Using Green Zirconium Oxide Layer and Organic Coating: An Efficient and Adherent Dual System. *Sustainability* **13**, 9688 (2021).
38. Liu, Q. et al. Investigation on adhesion strength and corrosion resistance of Ti-Zr aminotrimethylene phosphonic acid composite conversion coating on 7A52 aluminum alloy. *Appl. Surf. Sci.* **458**, 350–359 (2018).
39. Ghanbari, A. & Attar, M. M. Surface free energy characterization and adhesion performance of mild steel treated based on zirconium conversion coating: A comparative study. *Surf. Coat. Technol.* **246**, 26–33 (2014).
40. Golabadi, M., Aliofkhaezrai, M. & Toorani, M. Corrosion behavior of zirconium-pretreated/epoxy-coated mild steel: New approach for determination of cathodic disbondment resistance by electrochemical impedance spectroscopy. *J. Alloy. Compd.* **873**, 159800 (2021).
41. Wu, A.-H. et al. Corrosion resistance properties of colored zirconium conversion coating and powder coating on cold-rolled steel. *Rare Met.* **42**, 1005–1010 (2023).
42. Sababi, M., Terryn, H. & Mol, J. M. C. The influence of a Zr-based conversion treatment on interfacial bonding strength and stability of epoxy coated carbon steel. *Prog. Org. Coat.* **105**, 29–36 (2017).
43. Sharifi Golru, S., Attar, M. M. & Ramezanzadeh, B. Effects of surface treatment of aluminium alloy 1050 on the adhesion and anticorrosion properties of the epoxy coating. *Appl. Surf. Sci.* **345**, 360–368 (2015).
44. Han, X. et al. Corrosion resistance and microstructural characterization of Ti-Zr-V/waterborne resin composite conversion coating on 1060 aluminum alloy. *Colloids Surf. Physicochem. Eng. Asp.* **678**, 132503 (2023).
45. Andreatta, F. et al. SKPFM and SEM study of the deposition mechanism of Zr/Ti based pre-treatment on AA6016 aluminum alloy. *Surf. Coat. Technol.* **201**, 7668–7685 (2007).
46. De Nicolò, A. et al. Cerium conversion coating and sol-gel multilayer system for corrosion protection of AA6060. *Surf. Coat. Technol.* **287**, 33–43 (2016).

47. Živković, Lj. S., Jegdić, B. V., Popić, J. P., Bajat, J. B. & Mišković-Stanković, V. B. The influence of Ce-based coatings as pretreatments on corrosion stability of top powder polyester coating on AA6060. *Prog. Org. Coat.* **76**, 1387–1395 (2013).
48. Zhu, W., Li, W., Mu, S., Fu, N. & Liao, Z. Comparative study on Ti/Zr/V and chromate conversion treated aluminum alloys: Anti-corrosion performance and epoxy coating adhesion properties. *Appl. Surf. Sci.* **405**, 157–168 (2017).
49. Banjo, N., Sasaki, T. T. & Hono, K. Microstructural origin of adhesion and corrosion properties of Ti-based conversion coatings on A6063 alloy. *Appl. Surf. Sci.* **604**, 154411 (2022).
50. Sainis, S., Roşoiu, S., Ghassemali, E. & Zanella, C. The role of microstructure and cathodic intermetallics in localised deposition mechanism of conversion compounds on Al (Si, Fe, Cu) alloy. *Surf. Coat. Technol.* **402**, 126502 (2020).
51. Rodič, P., Kapun, B. & Milošev, I. Durable Polyacrylic/Siloxane-Silica Coating for the Protection of Cast AlSi7Mg0.3 Alloy against Corrosion in Chloride Solution. *Polymers* **15**, 3993 (2023).
52. Arrabal, R. et al. Pitting corrosion of rheocast A356 aluminium alloy in 3.5wt.% NaCl solution. *Corros. Sci.* **73**, 342–355 (2013).
53. Milošev, I., Kapun, B. & Rodič, P. The Relation Between the Microstructure of Aluminum Alloy 7075-T6 and the Type of Cerium Salt in the Formation of the Cerium Conversion Layer. *J. Electrochem. Soc.* **169**, 091501 (2022).
54. Buchheit, R. G., Grant, R. P., Hlava, P. F., McKenzie, B. & Zender, G. L. Local Dissolution Phenomena Associated with S Phase (Al_2CuMg) Particles in Aluminum Alloy 2024-T3. *J. Electrochem. Soc.* **144**, 2621–2628 (1997).
55. Gharbi, O. & Birbilis, N. Clarifying the Dissolution Mechanisms and Electrochemistry of Mg_2Si as a Function of Solution pH. *J. Electrochem. Soc.* **165**, C497 (2018).
56. Qi, J. et al. Formation of a Trivalent Chromium Conversion Coating on AA2024-T351 Alloy. *J. Electrochem. Soc.* **163**, C25 (2015).
57. Qi, J. et al. Chromate Formed in a Trivalent Chromium Conversion Coating on Aluminum. *J. Electrochem. Soc.* **164**, C442 (2017).
58. Denissen, P. J. & Garcia, S. J. Reducing subjectivity in EIS interpretation of corrosion and corrosion inhibition processes by in-situ optical analysis. *Electrochim. Acta* **293**, 514–524 (2019).
59. Milošev, I. et al. Siloxane polyacrylic sol-gel coatings with alkyl and perfluoroalkyl chains: Synthesis, composition, thermal properties and long-term corrosion protection. *Appl. Surf. Sci.* **574**, 151578 (2022).
60. Hamulić, D. et al. The Effect of the Methyl and Ethyl Group of the Acrylate Precursor in Hybrid Silane Coatings Used for Corrosion Protection of Aluminium Alloy 7075-T6. *Coatings* **10**, 172 (2020).
61. Rodič, P., Iskra, J. & Milošev, I. A hybrid organic-inorganic sol-gel coating for protecting aluminium alloy 7075-T6 against corrosion in Harrison's solution. *J. Sol.-Gel Sci. Technol.* **70**, 90–103 (2014).
62. Standard Test Methods for Rating Adhesion by Tape Test. <https://www.astm.org/d3359-23.html>.
63. Harb, S. V. et al. Organic-Inorganic Hybrid Coatings for Corrosion Protection of Metallic Surfaces. in *New Technologies in Protective Coatings* (eds. Giudice, C. & Canosa, G.) (InTech, 2017).
64. Fockaert, L. I. et al. Effect of zirconium-based conversion treatments of zinc, aluminium and magnesium on the chemisorption of ester-functionalized molecules. *Appl. Surf. Sci.* **508**, 145199 (2020).
65. Liu, T. et al. Machine learning assisted discovery of high-efficiency self-healing epoxy coating for corrosion protection. *Npj Mater. Degrad.* **8**, 1–11 (2024).
66. Schottner, G. Hybrid Sol-Gel-Derived Polymers: Applications of Multifunctional Materials. *Chem. Mater.* **13**, 3422–3435 (2001).
67. Pereira, G. S. et al. Cerium conversion coating and sol-gel coating for corrosion protection of the WE43 Mg alloy. *Corros. Sci.* **206**, 110527 (2022).
68. Li, L., Swain, G. P., Howell, A., Woodbury, D. & Swain, G. M. The Formation, Structure, Electrochemical Properties and Stability of Trivalent Chrome Process (TCP) Coatings on AA2024. *J. Electrochem. Soc.* **158**, C274 (2011).
69. Li, L., Kim, D. Y. & Swain, G. M. Transient Formation of Chromate in Trivalent Chromium Process (TCP) Coatings on AA2024 as Probed by Raman Spectroscopy. *J. Electrochem. Soc.* **159**, C326 (2012).
70. Guo, Y. & Frankel, G. S. Characterization of trivalent chromium process coating on AA2024-T3. *Surf. Coat. Technol.* **206**, 3895–3902 (2012).
71. Jolivet, J.-P. *Metal Oxide Nanostructures Chemistry: Synthesis from Aqueous Solutions*. (Oxford University Press, 2019). <https://doi.org/10.1093/oso/9780190928117.001.0001>.
72. Kraš, A., Milošev, I., Seyeux, A. & Marcus, P. Investigating the presence of tetrameric forms in the zirconium conversion coatings on cold-rolled steel: proof of concept. *npj Mater. Degrad.* (2024).
73. Osborne, J. H. Observations on chromate conversion coatings from a sol-gel perspective. *Prog. Org. Coat.* **41**, 280–286 (2001).
74. Pearlstein, F. & Agarwala, V. S. Trivalent chromium conversion coatings for aluminum. *Plat. Surf. Finish.* **July**, 50–55 (1994).
75. Xia, L. & McCreery, R. L. Chemistry of a Chromate Conversion Coating on Aluminum Alloy AA2024-T3 Probed by Vibrational Spectroscopy. *J. Electrochem. Soc.* **145**, 3083 (1998).
76. Zhong, X., Wu, X., Jia, Y. & Liu, Y. Self-repairing vanadium-zirconium composite conversion coating for aluminum alloys. *Appl. Surf. Sci.* **280**, 489–493 (2013).
77. Standard Practice for Operating Salt Spray (Fog) Apparatus. <https://www.astm.org/b0117-19.html>.

Acknowledgements

The authors would like to acknowledge student Veronika Bračič for her assistance in preparing the Zr-CrCC and sol-gel coatings and samples for testing. The funding was provided by the Slovenian Research and Innovation Agency (core programme funding No. P1-0134 and P2-0393). The authors acknowledge the Centre of Excellence in Nanoscience and Nanotechnology-Nanocenter, Ljubljana, Slovenia, to access the scientific equipment including FIB-SEM/EDXS. The company Talum d.d. is acknowledged for supplying the substrate plate (M-Era.Net grant COR_ID).

Author contributions

P.R. and I.M. conceptualised the work, P.R. conducted experimental work (synthesis of the sols, coatings preparation and deposition, electrochemical measurements, and data analysis), B.K. performed FIB-SEM/EDS analysis. P.R. and I.M. prepared and wrote the paper. All authors have read and agreed to the published version of the manuscript.

Competing interests

The authors declare no competing interests.

Additional information

Supplementary information The online version contains supplementary material available at <https://doi.org/10.1038/s41529-024-00467-5>.

Correspondence and requests for materials should be addressed to Ingrid Milošev.

Reprints and permissions information is available at <http://www.nature.com/reprints>

Publisher's note Springer Nature remains neutral with regard to jurisdictional claims in published maps and institutional affiliations.

Open Access This article is licensed under a Creative Commons Attribution 4.0 International License, which permits use, sharing, adaptation, distribution and reproduction in any medium or format, as long as you give appropriate credit to the original author(s) and the source, provide a link to the Creative Commons licence, and indicate if changes were made. The images or other third party material in this article are included in the article's Creative Commons licence, unless indicated otherwise in a credit line to the material. If material is not included in the article's Creative Commons licence and your intended use is not permitted by statutory regulation or exceeds the permitted use, you will need to obtain permission directly from the copyright holder. To view a copy of this licence, visit <http://creativecommons.org/licenses/by/4.0/>.

© The Author(s) 2024